LUND UNIVERSITY

Centrality determination of Pb-Pb collisions at root s(NN)=2.76 TeV with ALICE

Abelev, B.; Adam, J.; Adamova, D.; Adare, A. M.; Aggarwal, M. M.; Rinella, G. Aglieri;
Agnello, M.; Agocs, A. G.; Agostinelli, A.; Ahammed, Z.; Ahmad, N.; Masoodi, A. Ahmad; Ahn,
S. U.; Ahn, S. A.; Ajaz, M.; Akindinov, A.; Aleksandrov, D.; Alessandro, B.; Alici, A.; Alkin, A.;
Avina, E. Almaraz; Alme, J.; Alt, T.; Altini, V.; Altinpinar, S.; Altsybeev, I.; Andrei, C.; Andronic,
A.; Anguelov, V.; Anielski, J.; Anson, C.; Anticic, T.; Antinori, F.; Antonioli, P.; Aphecetche, L.;
Appelshaeuser, H.; Arbor, N.; Arcelli, S.; Arend, A.; Armesto, N.; Arnaldi, R.; Aronsson, T.;
Arsene, I. C.; Arslandok, M.; Asryan, A.; Augustinus, A.; Averbeck, R.; Awes, T. C.; Aeystoe,
J.; Azmi, M. D.

Link to publication

Centrality determination of Pb-Pb collisions at $\sqrt{s_{NN}} = 2.76$ TeV with ALICE

B. Abelev *et al.*[*]

(ALICE Collaboration)

(Received 22 January 2013; published 15 October 2013)

This publication describes the methods used to measure the centrality of inelastic Pb-Pb collisions at a center-of-mass energy of 2.76 TeV per colliding nucleon pair with ALICE. The centrality is a key parameter in the study of the properties of QCD matter at extreme temperature and energy density, because it is directly related to the initial overlap region of the colliding nuclei. Geometrical properties of the collision, such as the number of participating nucleons and the number of binary nucleon-nucleon collisions, are deduced from a Glauber model with a sharp impact parameter selection and shown to be consistent with those extracted from the data. The centrality determination provides a tool to compare ALICE measurements with those of other experiments and with theoretical calculations.

I. INTRODUCTION

Ultrarelativistic heavy-ion collisions at the Large Hadron Collider (LHC) produce strongly interacting matter under extreme conditions of temperature and energy density, similar to those prevailing in the first few microseconds after the Big Bang [1].

Since nuclei are extended objects, the volume of the interacting region depends on the impact parameter (*b*) of the collision, defined as the distance between the centers of the two colliding nuclei in a plane transverse to the beam axis. It is customary in the field of heavy-ion physics to introduce the concept of the centrality of the collision, which is directly related to the impact parameter and inferred by comparison of data with simulations of the collisions.

The purely geometrical Glauber model [2], which typically is used in this context, has its origins in the quantum mechanical model for *p-A* and *A-A* scattering described in Refs. [3–5]. The model treats a nuclear collision as a superposition of binary nucleon-nucleon interactions. The volume of the initial overlap region is expressed via the number of participant nucleons. A participant nucleon of one nucleus is defined as a nucleon that undergoes one or more binary collisions with nucleons of the other nucleus. The number of participants and spectators is defined as N_{part} and $N_{\text{spec}} = 2A - N_{\text{part}}$, where A is the total number of nucleons in the nucleus (mass number), and the number of binary collisions N_{coll} are calculated for a given value of the impact parameter and for a realistic initial distribution of nucleons inside the nucleus and assuming that nucleons follow straight trajectories. This approach provides a consistent description of *p-A*, *d-A*, and *A-A* collisions and is especially useful when comparing data from different experiments or from different collision systems and to theoretical calculations.

Neither the impact parameter nor geometrical quantities, such as N_{part}, N_{spec}, or N_{coll}, are directly measurable. Two experimental observables related to the collision geometry are the average charged-particle multiplicity N_{ch} and the energy carried by particles close to the beam direction and deposited in zero-degree calorimeters (ZDC), called the zero-degree energy E_{ZDC}. The average charged-particle multiplicity is assumed to decrease monotonically with increasing impact parameter. The energy deposited in the zero-degree calorimeters, E_{ZDC}, is directly related to the number of spectator nucleons N_{spec}, which constitute the part of the nuclear volume not involved in the interaction. However, unlike N_{ch}, E_{ZDC} does not depend monotonically on the impact parameter b because nucleons bound in nuclear fragments with similar magnetic rigidity as the beam nuclei remain inside the beam pipe and therefore are not detected in the ZDC. Since fragment formation is more important in peripheral collisions, the monotonic relationship between E_{ZDC} and b is valid only for relatively central events (small b). For this reason, the zero-degree energy measurement needs to be combined with another observable that is monotonically correlated with b.

The centrality is usually expressed as a percentage of the total nuclear interaction cross section σ [2]. The centrality percentile c of an *A-A* collision with an impact parameter b is defined by integrating the impact parameter distribution $d\sigma/db'$ as

$$c = \frac{\int_0^b d\sigma/db' \, db'}{\int_0^\infty d\sigma/db' \, db'} = \frac{1}{\sigma_{AA}} \int_0^b \frac{d\sigma}{db'} \, db'. \tag{1}$$

In ALICE, the centrality is defined as the percentile of the hadronic cross section corresponding to a particle multiplicity above a given threshold ($N_{\text{ch}}^{\text{THR}}$) or an energy deposited in the ZDC below a given value ($E_{\text{ZDC}}^{\text{THR}}$) in the ZDC energy distribution $d\sigma/dE_{\text{ZDC}}'$,

$$c \approx \frac{1}{\sigma_{AA}} \int_{N_{\text{ch}}^{\text{THR}}}^{\infty} \frac{d\sigma}{dN_{\text{ch}}'} \, dN_{\text{ch}}' \approx \frac{1}{\sigma_{AA}} \int_0^{E_{\text{ZDC}}^{\text{THR}}} \frac{d\sigma}{dE_{\text{ZDC}}'} \, dE_{\text{ZDC}}'. \tag{2}$$

---

[*]Full author list given at the end of the article.

The procedure can be simplified by replacing the cross section with the number of observed events, corrected for the trigger efficiency. However, at LHC energies, the strong electromagnetic fields generated by the heavy ions moving at relativistic velocity lead to large cross sections for QED processes [6–9]. Although the cross sections for these processes exceed those for the hadronic cross section by several orders of magnitude, they only contaminate the hadronic cross section in the most peripheral collisions. For this reason one may choose to restrict the centrality determination to the region where such contamination is negligible. The fraction of hadronic events excluded by such cut as well as the trigger efficiency can be estimated using a model of the nuclear collision and the related particle production.

In this paper, we report on the centrality determination used in the analyses of the Pb-Pb collision data from the 2010 and 2011 run recorded with the ALICE detector [10]. Specifically, the analysis presented here is done with a subset of the 2010 data, but the methods and results are valid for 2011 as well. In Sec. II, we describe the implementation of the Glauber model used by ALICE. We extract mean numbers of the relevant geometrical quantities for typical centrality classes defined by classifying the events according to their impact parameter. Section III describes the experimental conditions and the event selection with particular emphasis on the rejection of QED and machine-induced backgrounds. Section IV presents the methods employed by ALICE for the determination of the hadronic cross section, needed for the absolute determination of the centrality. The main method uses the VZERO amplitude distribution fitted with the Glauber model. The systematic uncertainty is obtained by comparing the fit to an unbiased VZERO distribution obtained by correcting the measured one by the efficiency of the event selection and the purity of the event sample. Section V presents the determination of the centrality classes using either the multiplicity at midrapidity or the energy deposited in the ZDC. We discuss the relation between the measured multiplicity and geometrical quantities connected to centrality, established by the Glauber model. These are nearly identical to those obtained in Sec. II, classifying the events according to their impact parameter, which are therefore used as reference in all ALICE analyses. Section VI presents the precision of the centrality determination in ALICE. Section VII summarizes and concludes the paper.

II. THE GLAUBER MODEL

The Glauber model is widely used to describe the dependence of $N_{\rm part}$ and $N_{\rm coll}$ on b in p-A, d-A, and A-A collisions [2–5]. The purpose of Monte Carlo implementations of the Glauber model [19,20] is to compose two nuclei from nucleons and simulate their collision process event by event. Geometrical quantities are calculated by simulating many nucleus-nucleus collisions. Mean values of these quantities are calculated for centrality classes defined by classifying the events according to their impact parameter b.

Following Ref. [21], the first step in the Glauber Monte Carlo is to prepare a model of the two nuclei by defining

stochastically the position of the nucleons in each nucleus. The nucleon position in the ^{208}Pb nucleus is determined by the nuclear density function, modeled by the functional form (modified Woods-Saxon or two-parameter Fermi distribution),

$$\rho(r) = \rho_0 \frac{1 + w(r/R)^2}{1 + \exp\left(\frac{r-R}{a}\right)}. \tag{3}$$

The parameters are based on data from low-energy electron-nucleus scattering experiments [22]. Protons and neutrons are assumed to have the same nuclear profile. The parameter ρ_0 is the nucleon density, which provides the overall normalization, not relevant for the Monte Carlo simulation; $R = (6.62 \pm 0.06)$ fm is the radius parameter of the ^{208}Pb nucleus; and $a = (0.546 \pm 0.010)$ fm is the skin thickness of the nucleus, which indicates how quickly the nuclear density falls off near the edge of the nucleus. The additional parameter w is needed to describe nuclei whose maximum density is reached at radii $r > 0$ ($w = 0$ for Pb). In the Monte Carlo procedure the radial coordinate of a nucleon is randomly drawn from the distribution $4\pi r^2 \rho(r)$ and ρ_0 is determined by the overall normalization condition $\int \rho(r)d^3r = A$. We require a hard-sphere exclusion distance of $d_{\rm min} = 0.4$ fm between the centers of the nucleons, i.e., no pair of nucleons inside the nucleus has a distance less than $d_{\rm min}$. The hard-sphere exclusion distance, characteristic of the length of the repulsive nucleon-nucleon force, is not known experimentally and thus is varied by 100% [$d_{\rm min} = (0.4 \pm 0.4)$ fm].

The second step is to simulate a nuclear collision. The impact parameter b is randomly selected from the geometrical distribution $dP/db \sim b$ up to a maximum $b_{\rm max} \simeq 20$ fm $> 2R_{\rm Pb}$. The maximum value of the impact parameter $b_{\rm max}$ is chosen large enough to simulate collisions until the interaction probability becomes zero. This is particularly important for the calculation of the total Pb-Pb cross section. The nucleus-nucleus collision is treated as a sequence of independent binary nucleon-nucleon collisions, where the nucleons travel on straight-line trajectories and the inelastic nucleon-nucleon cross section is assumed to be independent of the number of collisions a nucleon underwent previously, i.e., the same cross section is used for all successive collisions. Two nucleons from different nuclei are assumed to collide if the relative transverse distance between centers is less than the distance corresponding to the inelastic nucleon-nucleon cross section $d < \sqrt{\sigma_{NN}^{\rm inel}/\pi}$. A Gaussian overlap function can be used as an alternative to the black-disk nucleon-nucleon overlap function [23]. It makes no significant difference within systematic uncertainty in the global event properties.

The number of collisions $N_{\rm coll}$ and the number of participants $N_{\rm part}$ are determined by counting, respectively, the binary nucleon collisions and the nucleons that experience at least one collision. Following the notation in Ref. [2], the geometric nuclear overlap function T_{AA} is then calculated as $T_{AA} = N_{\rm coll}/\sigma_{NN}^{\rm inel}$ and represents the effective nucleon luminosity in the collision process.

For nuclear collisions at $\sqrt{s_{NN}} = 2.76$ TeV, we use $\sigma_{NN}^{\rm inel} = (64 \pm 5)$ mb, estimated by interpolation [11] of pp data at different center-of-mass energies and from cosmic rays [12,14] and subtracting the elastic-scattering cross section from the
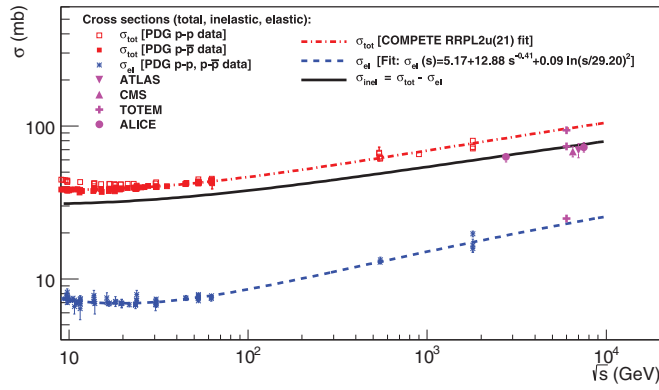
FIG. 1. (Color online) Compilation of total σ_{NN}^{tot}, elastic σ_{NN}^{el}, and inelastic $\sigma_{NN}^{\text{inel}}$ cross sections of pp and $p\bar{p}$ collisions [11–13]. The σ_{NN}^{el} curve is a fit performed by the COMPETE Collaboration also available at Refs. [12,14]. The pp data from ATLAS [15], CMS [16], TOTEM [17], and ALICE [18] agree well with the interpolation for $\sigma_{NN}^{\text{inel}}$.

total cross section. The interpolation is in good agreement with the ALICE measurement of the pp inelastic cross section at

$\sqrt{s_{NN}} = 2.76$ TeV, $\sigma_{NN}^{\text{inel}} = (62.8 \pm 2.4^{+1.2}_{-4.0})$ mb [18], and with the measurements of ATLAS [15], CMS [16], and TOTEM [17] at $\sqrt{s_{NN}} = 7$ TeV, as shown in Fig. 1.

The total Pb-Pb cross section is calculated as $\sigma_{\text{PbPb}} = N_{\text{evt}}(N_{\text{coll}} \geqslant 1)/N_{\text{evt}}(N_{\text{coll}} \geqslant 0) \times \pi b_{\text{max}}^2$, i.e., the geometrical value corrected by the fraction of events with at least one nucleon-nucleon collision. We obtain $\sigma_{\text{PbPb}} = (7.64 \pm 0.22(\text{syst.}))$ b, in agreement with the ALICE measurement $\sigma_{\text{PbPb}} = (7.7 \pm 0.1(\text{stat.})^{+0.6}_{-0.5}(\text{syst.}))$ b [9].

Table I reports the mean number of participants $\langle N_{\text{part}} \rangle$ and collisions $\langle N_{\text{coll}} \rangle$ and the mean nuclear thickness function $\langle T_{AA} \rangle$ for centrality classes defined by sharp cuts in the impact parameter b calculated with the Glauber model (Fig. 2). The root-mean-square (rms) of these distributions is a measure for the magnitude of the dispersion of the quantities.

The systematic uncertainties on the mean values are obtained by independently varying the parameters of the Glauber model within their estimated uncertainties. More specifically, the default value of the nucleon-nucleon cross section of $\sigma_{NN}^{\text{inel}} = 64$ mb was varied between 59 mb and 69 mb. The Woods-Saxon parameters were varied by one standard

TABLE I. Geometric properties (N_{part}, N_{coll}, and T_{AA}) of Pb-Pb collisions for centrality classes defined by sharp cuts in the impact parameter b (in fm). The mean values, the rms, and the systematic uncertainties are obtained with a Glauber Monte Carlo calculation.

| Centrality	$b_{\min}$ (fm)	$b_{\max}$ (fm)	$\langle N_{\text{part}} \rangle$	rms	(syst.)	$\langle N_{\text{coll}} \rangle$	rms	(syst.)	$\langle T_{AA} \rangle$ (1/mb)	rms (1/mb)	(syst.) (1/mb)
0–1%	0.00	1.57	403.8	4.9	1.8	1861	82	210	29.08	1.3	0.95
1–2%	1.57	2.22	393.6	6.5	2.6	1766	79	200	27.6	1.2	0.87
2–3%	2.22	2.71	382.9	7.7	3.0	1678	75	190	26.22	1.2	0.83
3–4%	2.71	3.13	372.0	8.6	3.5	1597	72	180	24.95	1.1	0.81
4–5%	3.13	3.50	361.1	9.3	3.8	1520	70	170	23.75	1.1	0.81
5–10%	3.50	4.94	329.4	18	4.3	1316	110	140	20.56	1.7	0.67
10–15%	4.94	6.05	281.2	17	4.1	1032	91	110	16.13	1.4	0.52
15–20%	6.05	6.98	239.0	16	3.5	809.8	79	82	12.65	1.2	0.39
20–25%	6.98	7.81	202.1	16	3.3	629.6	69	62	9.837	1.1	0.30
25–30%	7.81	8.55	169.5	15	3.3	483.7	61	47	7.558	0.96	0.25
30–35%	8.55	9.23	141.0	14	3.1	366.7	54	35	5.73	0.85	0.20
35–40%	9.23	9.88	116.0	14	2.8	273.4	48	26	4.272	0.74	0.17
40–45%	9.88	10.47	94.11	13	2.6	199.4	41	19	3.115	0.64	0.14
45–50%	10.47	11.04	75.3	13	2.3	143.1	34	13	2.235	0.54	0.11
50–55%	11.04	11.58	59.24	12	1.8	100.1	28	8.6	1.564	0.45	0.082
55–60%	11.58	12.09	45.58	11	1.4	68.46	23	5.3	1.07	0.36	0.060
60–65%	12.09	12.58	34.33	10	1.1	45.79	18	3.5	0.7154	0.28	0.042
65–70%	12.58	13.05	25.21	9.0	0.87	29.92	14	2.2	0.4674	0.22	0.031
70–75%	13.05	13.52	17.96	7.8	0.66	19.08	11	1.3	0.2981	0.17	0.020
75–80%	13.52	13.97	12.58	6.5	0.45	12.07	7.8	0.77	0.1885	0.12	0.013
80–85%	13.97	14.43	8.812	5.2	0.26	7.682	5.7	0.41	0.12	0.089	0.0088
85–90%	14.43	14.96	6.158	3.9	0.19	4.904	4.0	0.24	0.076 62	0.062	0.0064
90–95%	14.96	15.67	4.376	2.8	0.10	3.181	2.7	0.13	0.0497	0.042	0.0042
95–100%	15.67	20.00	3.064	1.8	0.059	1.994	1.7	0.065	0.031 15	0.026	0.0027
0–5%	0.00	3.50	382.7	17	3.0	1685	140	190	26.32	2.2	0.85
5–10%	3.50	4.94	329.4	18	4.3	1316	110	140	20.56	1.7	0.67
10–20%	4.94	6.98	260.1	27	3.8	921.2	140	96	14.39	2.2	0.45
20–40%	6.98	9.88	157.2	35	3.1	438.4	150	42	6.850	2.3	0.23
40–60%	9.88	12.09	68.56	22	2.0	127.7	59	11	1.996	0.92	0.097
60–80%	12.09	13.97	22.52	12	0.77	26.71	18	2.0	0.4174	0.29	0.026
80–100%	13.97	20.00	5.604	4.2	0.14	4.441	4.4	0.21	0.069 39	0.068	0.0055
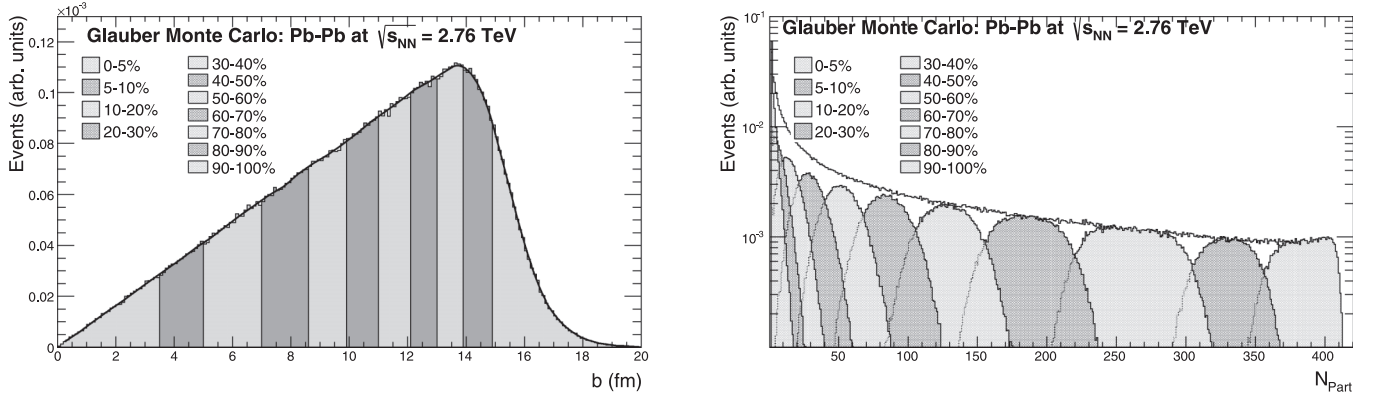
FIG. 2. Geometric properties of Pb-Pb collisions at $\sqrt{s_{NN}} = 2.76$ TeV obtained from a Glauber Monte Carlo calculation: impact parameter distribution (left), sliced for percentiles of the hadronic cross section, and distributions of the number of participants (right) for the corresponding centrality classes.

deviation to determine uncertainties related to the nuclear density profile. The minimum distance of 0.4 fm between two nucleons of the same nucleus was varied by 100%, from 0 to 0.8 fm, to evaluate the effects of a nucleon hard core (as mentioned above). Figure 3 shows the resulting variations for Pb-Pb collisions at $\sqrt{s_{NN}} = 2.76$ TeV. The total systematic uncertainty reported in Table I was obtained by adding in quadrature the deviations from the default result for each of the variations listed above. The uncertainty of N_{part} ranges from about 3–4% in peripheral collisions to <1% in central collisions, the uncertainty of N_{coll} ranges from about 7% in peripheral collisions to about 11% in central collisions, and the uncertainty of T_{AA} ranges from about 6% in peripheral collisions to about 3% in central collisions. The nuclear overlap function T_{AA} is often used to compare observables related to hard processes in A-A and pp collisions. Since $T_{AA} = N_{coll}/\sigma_{NN}^{inel}$, it has the same systematic uncertainties as N_{coll} except that the uncertainty on σ_{NN}^{inel} cancels out.

Finally, it is worth noting that more sophisticated implementations of the Glauber model [23–25] suggest that effects not included in our Glauber model, such as the changes of the excluded volume on the nuclear density and two-body correlations, can be approximated by slightly adjusting the Woods-Saxon parameters. The modified parameters, however,

are well covered by the systematic uncertainty quoted above for the parameters that we use.

III. EXPERIMENTAL CONDITIONS

A. The ALICE detector

ALICE is an experiment dedicated to the study of heavy-ion collisions at the LHC. A detailed description of the apparatus is given in Ref. [10]. Here we briefly describe the detector components used in this analysis.

The Silicon Pixel Detector (SPD) is the innermost part of the Inner Tracking System (ITS). It consists of two cylindrical layers of hybrid silicon pixel assemblies positioned at average radial distances of 3.9 and 7.6 cm from the beam line, with a total of 9.8×10^6 pixels of size 50×425 μm^2, read out by 1200 electronic chips. The SPD coverage for particles originating from the center of the detector is $|\eta| < 2.0$ and $|\eta| < 1.4$ for the inner and outer layers, respectively. Each chip provides a fast signal if at least one of its pixels is hit. The signals from the 1200 chips are combined in a programmable logic unit which supplies a trigger signal. The fraction of SPD channels active during 2010 data taking was 70% for the inner and 78% for the outer layers.
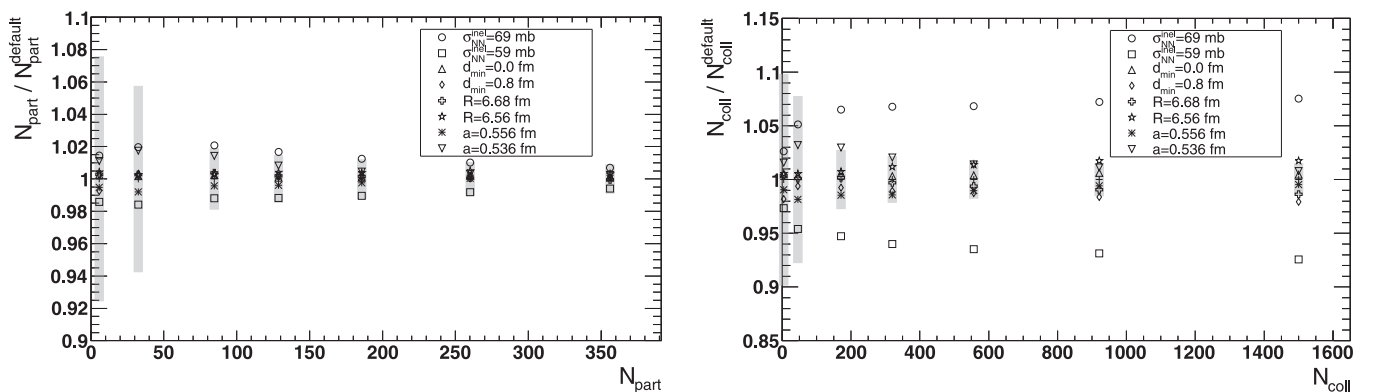

FIG. 3. Sensitivity of N_{part} (left) and N_{coll} (right) to variations of parameters in the Glauber Monte Carlo model of Pb-Pb collisions at $\sqrt{s_{NN}} = 2.76$ TeV. The gray band represents the rms of N_{part} and N_{coll}, respectively. It is scaled by a factor 0.1 for visibility.

The VZERO detector consists of two arrays of 32 scintillator cells placed at distances $z = 3.4$ m and $z = -0.9$ m from the nominal interaction point, along the beam line, covering the full azimuth. The VZERO detector is within $2.8 < \eta < 5.1$ (VZERO-A) and $-3.7 < \eta < -1.7$ (VZERO-C). Both amplitude and time of signals in each scintillator are recorded. The VZERO time resolution is better than 1 ns, allowing discrimination of beam-beam collisions from background events produced upstream of the experiment. The VZERO is also used to provide a trigger signal (see Sec. III B).

The Time Projection Chamber (TPC) is used for charged-particle trajectory reconstruction, track momentum measurement, and particle identification. The ALICE TPC is a large cylindrical drift detector whose active volume extends radially from 85 to 247 cm and from -250 to $+250$ cm along the beam direction. The active volume of nearly 90 m^3 is filled with a gas mixture of Ne (85.7%), CO_2 (9.5%), and N_2 (4.8%) until the end of 2010 and Ne (90%) and CO_2 (10%) since the beginning of 2011. A central electrode maintained at -100 kV divides the TPC into two sections. The end caps are equipped with multiwire proportional chambers with cathode pad readout. For a particle traversing the TPC up to 159 position signals (clusters) are recorded. The cluster data are used to reconstruct the charged-particle trajectory as well as to calculate the particle's specific energy loss used to identify the species of the particle which has produced the track.

The two ZDCs in the ALICE experiment measure the energy of spectator (noninteracting) nucleons: ZP measures protons and ZN measures neutrons. They are situated about 114 m from the interaction point on each side of the experiment [10]. Each ZDC consists of two quartz fiber sampling calorimeters: the neutron calorimeter, positioned between the two beam pipes downstream of the first machine dipole that separates the two charged-particle beams, and the proton calorimeter, positioned externally to the outgoing beam pipe. The energy resolution at beam energy is estimated to be 20% for the neutron (20.0% for ZNC, 21.2% for ZNA) and 24% for the proton calorimeters, respectively.

B. Data set and online event selection

During the first LHC Pb-Pb run in 2010, beams of four bunches with about 10^7 Pb ions per bunch collided at $\sqrt{s_{NN}} = 2.76$ TeV, with an estimated luminosity of 5×10^{23} cm^{-2} s^{-1}. ALICE collected about 90 million nuclear collision events using different interaction triggers with increasingly tighter conditions. These triggers used VZERO and SPD detector signals in coincidence with a bunch crossing corresponding to a beam-beam collision:

V0AND: signals in VZERO-A and VZERO-C;
3-out-of-3: signals in VZERO-A and VZERO-C and at least two chips hit in the outer layer of the SPD;
2-out-of-3: two of the three conditions listed above.

The threshold in the VZERO detector for each of the VZERO tiles corresponded approximately to the energy deposition of one minimum ionizing particle.

Control events were also collected with the same trigger logic, in coincidence with only one beam crossing the ALICE interaction point (from either the A or the C side) or with no beam at all ("empty"). The luminous region had an rms width of 5.9 cm in the longitudinal direction and 50 μm in the transverse direction. For the estimated luminosity, using the least selective of the interaction triggers, the observed rate was about 50 Hz. This was mainly due to electromagnetically induced processes [26]. These processes have large cross sections at LHC energies but generate low multiplicities and therefore do not contribute to the typical particle multiplicities of interest for the present paper. The trigger rate without beam was negligible and the rate in coincidence with bunches of only one beam was about 1 Hz. The probability for collision pile-up per triggered event was less than 10^{-4}.

C. Offline event selection

The offline event selection is applied with the purpose of selecting hadronic interactions with the highest possible efficiency, while rejecting the machine-induced and physical backgrounds. The offline event selection replays the on-line trigger condition, using the same quantities calculated offline, so events triggered by noise in the SPD are discarded, and the weighted time average over all channels is used for the VZERO, leading to a better time resolution. In addition, the offline event selection rejects the machine-induced background and parasitic collisions. This contamination amounts to about 25% of all collected events. To keep the conditions of all detectors as uniform as possible (in particular those around midrapidity, such as the SPD), the centrality analysis was restricted to a region around the vertex, $|z_{\text{vtx}}| \lesssim 10$ cm.

1. Machine-induced background

One source of machine-induced background is due to beam-gas events, caused by one of the beams interacting with the residual gas in the beam pipe; another source of background are events where ions in the beam halo interact with mechanical structures in the machine. These interactions mostly occur outside of the interaction region and thus produce a signal that is "too early" in the same-side VZERO, compared to a collision that occurs in the nominal interaction region between the VZERO detectors. Therefore these events can be rejected using the timing information of the VZERO. This is illustrated in Fig. 4 which shows the arrival time of particles at the VZERO-A detector relative to the nominal beam crossing time. Beam-halo or beam-gas interactions are visible as secondary peaks in the time distribution because particles produced in background interactions arrive at earlier times in the detector relative to particles produced in beam-beam collisions at the nominal vertex, which are the majority of the signals. Other small peaks between these main ones arise from satellite collisions.

Another source of machine-induced background is due to parasitic collisions from debunched ions. The radiofrequency (RF) structure of the LHC of 400 MHz is such that there are 10 equidistant RF buckets within the 25-ns time interval between two possible nominal bunch positions. Therefore the
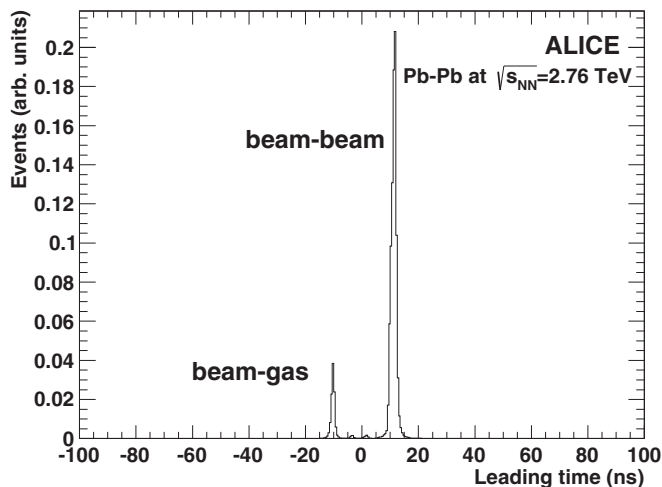
FIG. 4. Time distribution of signals in the VZERO detector on the A side. The peaks corresponding to beam-beam, beam-gas, and satellite collision events are clearly visible.

buckets are spaced by 2.5 ns. Only one of them should be populated by ions [27]. However, ions can "jump" into one of the neighboring buckets. Therefore collisions occur either between ions in the nominal RF buckets but also between one or two ions displaced by one or more RF buckets. This causes a displacement in the Z-vertex position of 2.5 ns/$2c$ = 37.5 cm, well outside the fiducial region $|z_{vtx}| \lesssim 10$ cm. Those events are thus to be considered as "background" and are rejected using the correlation between the sum and the difference of times measured in each of the neutron ZDCs, as shown in Fig. 5. Such satellite collisions can also be rejected using the vertex cut.
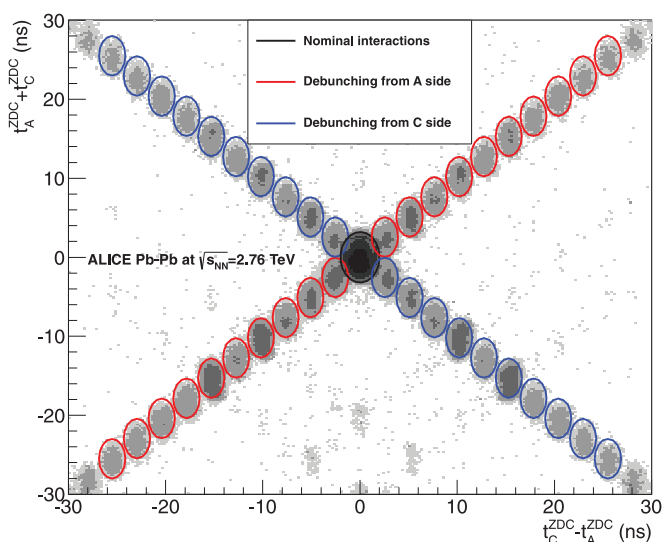

FIG. 5. (Color online) Correlation between the sum and the difference of times recorded by the neutron ZDC on either side of the interaction region. The large cluster in the middle corresponds to collisions between ions in the nominal RF buckets of each beam, while the small clusters along the diagonals (spaced by 2.5 ns in the time difference) correspond to collisions in which one of the ions is displaced by one or more RF buckets.

After the event selection, the remaining machine-induced background, estimated from the control triggers (i.e., triggers that fire for coincidences between empty and filled or empty and empty bunches), is negligible.

2. Electromagnetic interaction background

At the LHC energy, the cross sections for electromagnetic (EM) processes, generated by the EM fields of relativistic heavy ions, are enormous [$\mathcal{O}$(kbarn)] [6–9]. This is the main physical background and needs to be rejected in heavy-ion collisions to isolate hadronic interactions. QED processes consist of: photo-production and photo-nuclear interactions. Photo-production results in the creation of an e^+e^- pair. Photo-nuclear interactions, where one photon from the EM field of one of the nuclei interacts with the other nucleus, possibly fluctuating to a vector meson, yield a low multiplicity of soft particles in the ALICE central barrel. In the case of single photoproduction, the particle multiplicity is asymmetric within the event. Along the beam direction, the electromagnetic dissociation (EMD) cross sections are large resulting in a non-negligible probability for one neutron emission from either nucleus.

The EMD cross sections have been measured in a special run triggering on a signal in one of the neutron ZDCs, ZNA or ZNC, with a threshold placed well below the single-neutron signal to detect the neutrons from giant dipole resonance (GDR) decay emitted very close to beam rapidity [9]. The recorded event sample is dominated by electromagnetic dissociation of one or both nuclei measured to be $\sigma^{\text{single EMD}} = 187.4 \pm 0.2(\text{stat.})^{+13.2}_{-11.2}(\text{syst.})$ b compared to the mutual EMD cross section of $\sigma^{\text{mutual EMD}} = 5.7 \pm 0.1(\text{stat.}) \pm 0.4(\text{syst.})$ b. The single EMD events can be clearly identified when correlating the response of ZNA and ZNC (Fig. 6). The additional requirement of a signal in an electromagnetic calorimeter close to beam rapidity (ZEM) allows one to distinguish between mutual EMD and hadronic interaction events.
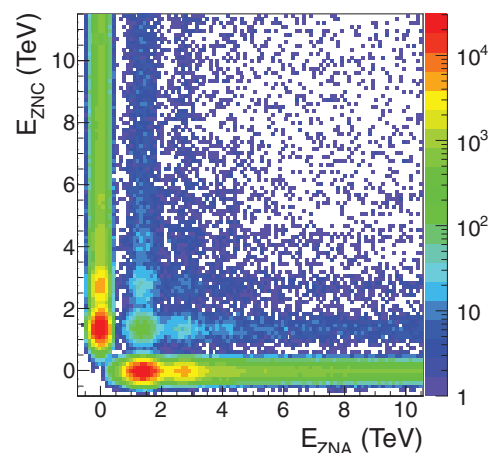

FIG. 6. (Color online) Correlation between signals in the two neutron zero-degree calorimeters, ZNA and ZNC. The figure is taken from Ref. [9]. Single electromagnetic dissociation events produce signal in only one of the calorimeters. Mutual dissociation and hadronic interactions populate interior of the plot and can be distinguished from each other by the signal in ZEM.

In order to reduce the contribution due to single-neutron emission, we require a ZDC signal three standard deviations above the single-neutron peak. This selection rejects about 3% of all events within 10 cm from the nominal interaction point after removal of beam-gas and parasitic collisions and only removes events for peripheral collisions (in the 90–100% region). The coincidence of the ZDC signals rejects all the single-neutron emission events. The simultanous emissions from both nuclei still are accepted, which, however, are only relevant for very peripheral collisions.

For systematic studies, another selection based on the information from the TPC is used, where at least one track reconstructed in the TPC is requested in order to keep the event. This selection removes few peripheral hadronic interactions and strongly suppresses the EM background.

IV. DETERMINATION OF THE HADRONIC CROSS SECTION

In order to classify the collisions in percentiles of the hadronic cross section using the charged-particle multiplicity, it is necessary to know the particle multiplicity at which the purity of the event sample and the efficiency of the event selection becomes 100%. We define the *anchor point* (AP) as the amplitude of the VZERO detector equivalent to 90% of the hadronic cross section, which determines the absolute scale of the centrality. The determination of the AP requires the knowledge of the trigger efficiency and the remaining background contamination in nuclear collision events. Two methods have been used to study this. The difference in the results obtained with the two methods is used to estimate the systematic uncertainty by the following:

Simulating the multiplicity distribution (see Sec. IV A). In the first approach, we use a full simulation of hadronic and EM processes, including a detailed description of the detector response, to study the efficiency of the event selection (Sec. IV A1) and to estimate the background contamination (Sec. IV A2). The real multiplicity distribution, corrected for efficiency and purity, allows direct access to the AP.

Fitting the multiplicity distribution (see Sec. IV B). In the second method, we use the Glauber Monte Carlo, combined with a simple model for particle production, to simulate a multiplicity distribution which is then compared to the experimental one. The simulated distribution describes the experimental one down to the most peripheral events where they start to deviate due to background contamination and limited trigger efficiency. The location of the divergence between the data and simulation can be used to define the AP.

The centrality determination is performed for different trigger and detector settings. The different triggers change the fraction of accepted events from EM processes, which determines the shape of the multiplicity distribution for very peripheral collisions below the AP. The position of the AP is very stable for the entire 2010 (and 2011) run period and does not change within the quoted systematic uncertainty discussed below. Small variations in detector conditions induce small changes in the position of the edge of the multiplicity distribution for most central events. Nevertheless, the centrality determination, adjusted to account for small changes in the detector configuration, provides a stable centrality selection for the entire data-taking period (the mean fraction of events in the 0–1% bin is 0.01 with a rms of 0.001, and in the 40–50% bin the mean fraction is 0.101 with an rms of 0.002).

A. Method 1: Correcting the multiplicity distribution

With this method the AP is determined by evaluating the efficiency of the event selection and by estimating the purity of the obtained event sample.

1. Efficiency of the event selection

The efficiency for the different event selections is studied with simulations of hadronic reactions and with dedicated pp runs. For simulations we use HIJING [28] or AMPT [29] with a full GEANT [30] description of the ALICE detector and a trigger emulator. In the simulations the efficiency is defined as the ratio of events selected by a given condition to all generated events. In the two dedicated pp runs, which were taken at the end of the 2010 run at $\sqrt{s} = 7$ TeV, the detector conditions were similar to those in the Pb-Pb run. The VZERO gain was adjusted such that the response to minimum ionizing particles (MIP) corresponded to three ADC channels for one run or six for the other run. For the Pb-Pb run, it was set to four channels, i.e., between the two tested conditions. In the special pp runs, we used a minimum interaction trigger, which requires a logical OR between a hit in the SPD and in either of the two VZERO detectors (CINT1 trigger condition). The same event selection criteria as used in the Pb-Pb run as the trigger have been applied. The relative event selection efficiency is defined as the ratio of events selected by a given condition to all the events recorded with the pp minimum-bias interaction trigger (CINT1). Since the pp minimum-bias interaction trigger (CINT1) has an efficiency that is effectively 100% for nondiffractive events [18], the relative efficiency measured in the pp runs, shown in Fig. 7, can be qualitatively compared to that obtained in Pb-Pb simulations with $N_{\text{part}} = 2$. Except for very low amplitudes, results from HIJING and AMPT are in very good agreement. AMPT predicts a slightly higher efficiency (about 0.5%), as a consequence of the broader rapidity distribution. The comparison with the pp runs shows a reasonable agreement for the "MIP = 6" case, while the "MIP = 3" is clearly lower.

For the Pb-Pb run, the efficiency of the event selection is calculated using the average of results obtained with HIJING and AMPT. The efficiency of the interaction triggers is 99.4%, 97.1%, and 96.9%, respectively, for 2-out-of-3, V0AND, and 3-out-of-3 using HIJING and 99.7%, 98.6%, and 98.4% using AMPT. The line in Fig. 7, corresponding to the 90% of the hadronic cross section shows that the trigger is always fully efficient for the 90% most central collisions, except for the "MIP = 3" pp case, where the efficiency is 95%.

2. Remaining contamination

The purity of the data sample passing a given event selection is estimated using HIJING simulations [28] for
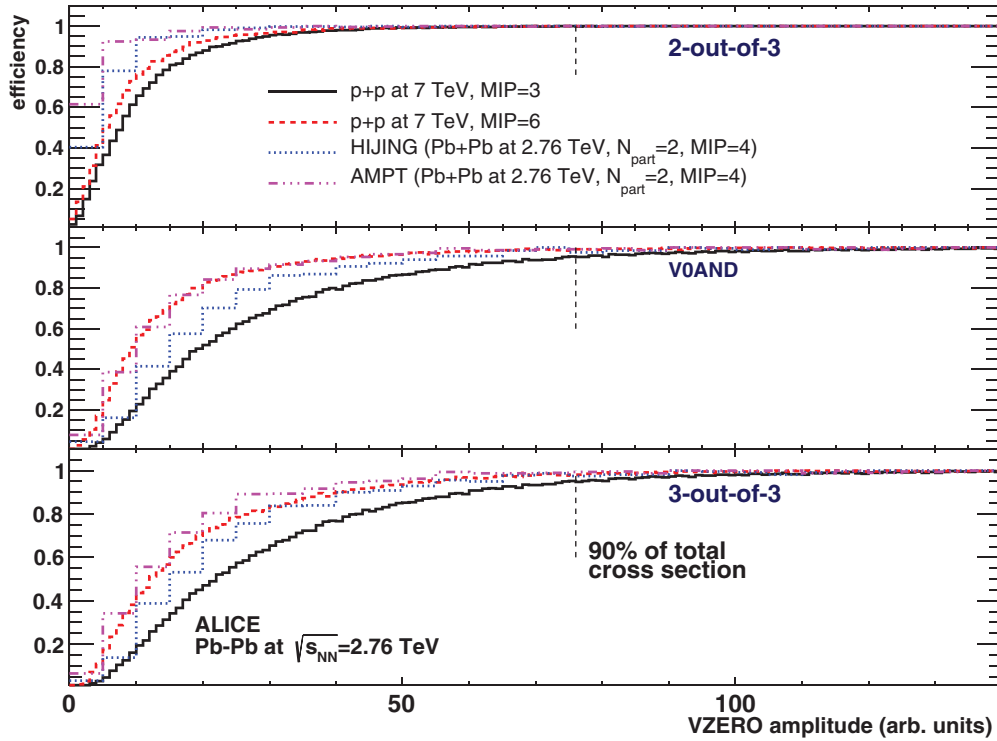
FIG. 7. (Color online) Efficiency of the three online triggers (2-out-of-3, V0AND, and 3-out-of-3) used for Pb-Pb collisions as a function of the VZERO amplitude calculated with HIJING and AMPT and measured in dedicated *pp* runs. The efficiency in the simulation has been calculated for events with $N_{\text{part}} = 2$.

hadronic processes and QED [8] and STARLIGHT [7] for the simulations of the EM background. For the electromagnetic dissociation we assume that the selection based on the signal 3σ above the single-neutron peak in the ZDCs (see Sec. III C2) is fully efficient.

In Fig. 8, data taken with the V0AND interaction trigger are compared to the sum of HIJING and background (QED + STARLIGHT) simulations with the same event selection. The simulations are scaled to the known cross sections as follows:

HIJING (hadronic): $\sigma_H = 7.66$ b [28];
QED (EM): $\sigma_Q = 92$ kb [8];
STARLIGHT (single-neutron dissociation): $\sigma_{\text{SNS}} = 24.2$ b [7];
STARLIGHT (double-neutron dissociation): $\sigma_{\text{SND}} = 240$ mb [7].

The sum of the simulations is normalized to the data in the region $150 <$ VZERO amplitude < 500, where there is no background contamination. The contribution from QED is completely removed by the V0AND trigger. The dashed lines, indicating, respectively, 80% and 90% of the hadronic cross section, show that there is no significant background contamination for collisions more central than 90%. The region 90–100% is reasonably understood as the agreement between data and simulation is quite good. The remaining discrepancy between the data and the sum of all contributions is included in the systematic uncertainty.

To assign a systematic uncertainty, the comparison is made for the three online interaction triggers and other event selections requiring (i) V0AND + TPC(one track fully reconstructed in the TPC on top of the V0AND trigger) and (ii) V0AND + ZDC(3σ cut above single-neutron peak in ZDC on top of the V0AND trigger). For all these variations a cross section is calculated and the difference is included in the systematic uncertainty.

Figure 9 shows the purity of the various Pb-Pb event samples after those selections. The purity, plotted as a function
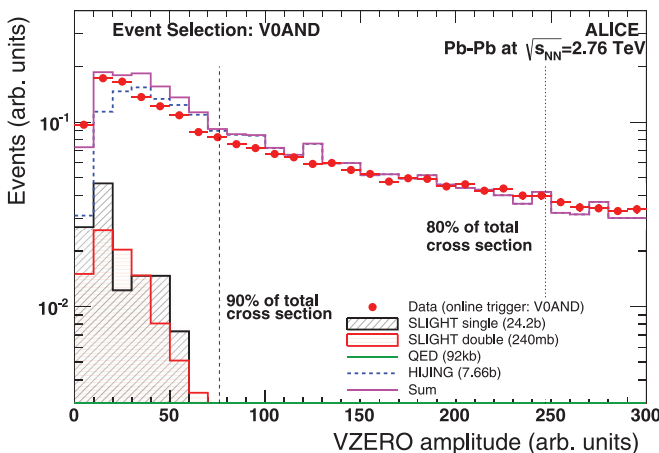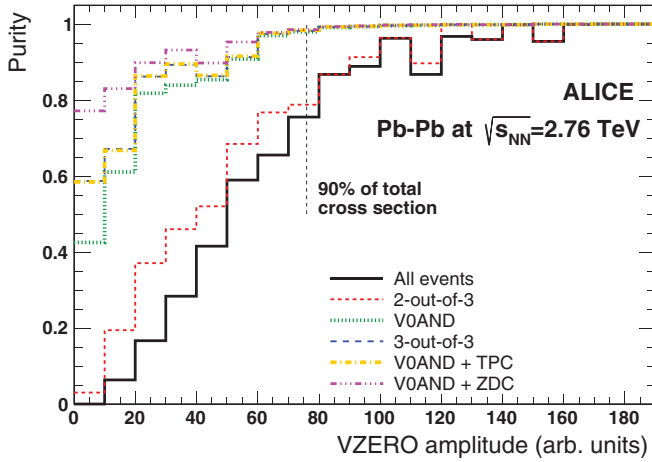

FIG. 8. (Color online) VZERO amplitude distribution in data (red points) and simulations with the V0AND interaction trigger. The data are compared to the sum of HIJING + QED + STARLIGHT simulations (histogram) with the same event selection.

FIG. 9. (Color online) Purity of the three online interaction triggers (2-out-of-3, V0AND, and 3-out-of-3) and other event selections used for Pb-Pb collisions as a function of the VZERO amplitude calculated with HIJING, STARLIGHT, and QED simulations. The dashed line indicates 90% of the hadronic cross section.

of the VZERO amplitude (V), is defined as the fraction of hadronic collisions over all the events selected with a given condition,

$$\text{purity} = \frac{\frac{dN_x}{dV}\big|_H \frac{\sigma_H}{N_H}}{\frac{dN_x}{dV}\big|_H \frac{\sigma_H}{N_H} + \frac{dN_x}{dV}\big|_{\text{SNS}} \frac{\sigma_{\text{SNS}}}{N_{\text{SNS}}} + \frac{dN_x}{dV}\big|_{\text{SND}} \frac{\sigma_{\text{SND}}}{N_{\text{SND}}} + \frac{dN_x}{dV}\big|_Q \frac{\sigma_Q}{N_Q}},$$

(4)

where σ_x and N_x are the cross sections and number of events for a given process, x, where $x = H$, SNS, SND, and Q, for HIJING, STARLIGHT single, STARLIGHT double, and QED, respectively.

The purity of the event sample can be verified using the correlation of the energy deposition in the two sides of the ZN calorimeter, similar to the one shown in Fig. 6. Single-neutron peaks are visible in the 80–90% centrality class, which may indicate some remaining contamination from EMD events. However, their origin can be also attributed to asymmetric Pb-Pb events, as well as a pile-up of an EMD and a hadronic collision. Since this contamination cannot be easily removed, analyses that use peripheral classes like 80–90% assign an additional 6% systematic uncertainty on the event selection to take into account the possible contamination from EMD.

B. Method 2: Fitting the multiplicity distribution

Another independent way to define the AP uses a phenomenological approach based on the Glauber Monte Carlo to fit the experimental multiplicity distribution. The Glauber Monte Carlo uses the assumptions mentioned above plus a convolution of a model for particle production, based on a negative binomial distribution (NBD). This latter assumption is motivated by the fact that in minimum bias pp and $p\overline{p}$ collisions at high energy, the charged-particle multiplicity $d\sigma/dN_{\text{ch}}$ has been measured over a wide range of rapidity and is well described by a NBD [31,32]. This approach allows one to simulate an experimental multiplicity distribution (e.g.,
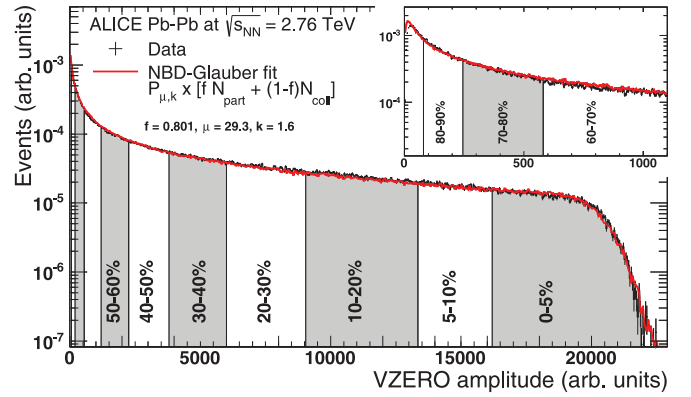

FIG. 10. (Color online) Distribution of the sum of amplitudes in the VZERO scintillators. The distribution is fitted with the NBD-Glauber fit (explained in the text), shown as a line. The centrality classes used in the analysis are indicated in the figure. The inset shows a zoom of the most peripheral region.

VZERO amplitude), which can be compared with the one from data.

Figure 10 shows the distribution of VZERO amplitudes for all events triggered with the 3-out-of-3 trigger (see Sec. III B) after removing the beam background (see Sec. III C1), part of the EM background with the ZDC cut (see Sec. III C2), and a Z-vertex cut $|z_{\text{vtx}}| < 10$ cm. The multiplicity distribution has the classical shape of a peak corresponding to most peripheral collisions (contaminated by EM background and by missing events due to the trigger inefficiency), a plateau of the intermediate region, and an edge for the central collisions, which is sensitive to the intrinsic fluctuations of N_{part} and $dN_{\text{ch}}/d\eta$ and to detector acceptance and resolution.

The Glauber Monte Carlo defines, for an event with a given impact parameter b, the corresponding N_{part} and N_{coll}. The particle multiplicity per nucleon-nucleon collision is parametrized by a NBD. To apply this model to any collision with a given N_{part} and N_{coll} value we introduce the concept of "ancestors," i.e., independently emitting sources of particles. We assume that the number of ancestors $N_{\text{ancestors}}$ can be parameterized by $N_{\text{ancestors}} = f N_{\text{part}} + (1 - f)N_{\text{coll}}$. This is inspired by two-component models [33,34], which decompose nucleus-nucleus collisions into soft and hard interactions, where the soft interactions produce particles with an average multiplicity proportional to N_{part}, and the probability for hard interactions to occur is proportional to N_{coll}. We discuss the independence of the fit results of this assumption below (Sec. IV B1).

To generate the number of particles produced per interaction, we use the negative binomial distribution

$$P_{\mu,k}(n) = \frac{\Gamma(n+k)}{\Gamma(n+1)\Gamma(k)} \frac{(\mu/k)^n}{(\mu/k+1)^{n+k}},$$

(5)

which gives the probability of measuring n hits per ancestor, where μ is the mean multiplicity per ancestor and k controls the width. For every Glauber Monte Carlo event, the NBD is sampled $N_{\text{ancestors}}$ times to obtain the averaged simulated VZERO amplitude for this event, which is proportional to the number of particles hitting the hodoscopes. The VZERO

amplitude distribution is simulated for an ensemble of events and for various values of the NBD parameters μ and k and the $N_{\text{ancestors}}$ parameter f. A minimization procedure is applied to find the parameters which result in the smallest χ^2, also shown in Fig. 10. The fit is performed for VZERO amplitudes large enough so the purity of the event sample and the efficiency of the event selection is 100%. That leaves a very broad range in the amplitude values that can be fitted to extract parameters f, μ, and k directly from the data. The amplitude, above which we have 90% of the hadronic cross section, defines the AP. The quality of the fit is good, as the χ^2/NDF is approximately unity for all fits. We note that the high-multiplicity tail, which is quite sensitive to fluctuations and the detector resolution not implemented in the model, is not perfectly well described. Even replacing the black-disk nucleon-nucleon overlap function with a Gaussian does not improve the fit, as the difference in the N_{part} distribution is washed out in the N_{ch} distribution. However, it is important to remark that the fit is used solely to determine the AP, which is quite insensitive to the detailed shape of the high-multiplicity tail.

An equivalent procedure was applied to fit, with the NBD-Glauber method, the distribution of the hits collected in the outer layer of the SPD, and the tracks reconstructed in the TPC. All these analyses give consistent results, which are summarized in Sec. IV C.

1. Ancestor dependence

The number of emitting sources $N_{\text{ancestors}}$ is determined by a function inspired by the two-component models, i.e., $N_{\text{ancestors}} = f N_{\text{part}} + (1 - f) N_{\text{coll}}$. However, other assumptions can be made, leading to a different parametrization, which are briefly discussed in the following. The ancestor dependence on N_{part} and N_{coll} derives from a parametrization of the dependence of the charged-particle multiplicity on N_{part} and N_{coll}. Systematic studies of this dependence performed at the SPS [36–38], at RHIC [39], and recently at the LHC [35,40,41] have been used in an attempt to constrain different models of particle production.

The charged-particle multiplicity is expected to scale with N_{part} in scenarios dominated by soft processes. In this case, all the participant nucleons can be assumed to contribute with the same amount of energy to particle production, and the scaling with N_{part} is approximately linear. By contrast, a scaling with N_{coll} is expected for nuclear collisions in an energy regime where hard processes dominate over soft particle production. In this case, nuclear collisions can be considered as a superposition of binary nucleon-nucleon collisions. Two-component models are used to quantify the relative importance of soft and hard processes in the particle production mechanism at different energies.

To determine the scaling behavior of the particle production, the charged-particle multiplicity $dN_{\text{ch}}/d\eta$ as a function of the number of participants N_{part} was fitted with a power-law function of N_{part}, i.e., $dN_{\text{ch}}/d\eta \propto N_{\text{part}}^{\alpha}$. While at SPS energy the scaling with N_{part} is approximately linear, i.e., $\alpha \sim 1$ [36–38], results from the experiments at RHIC show evidence of a large contribution of hard processes to particle production, resulting in $\alpha > 1$.
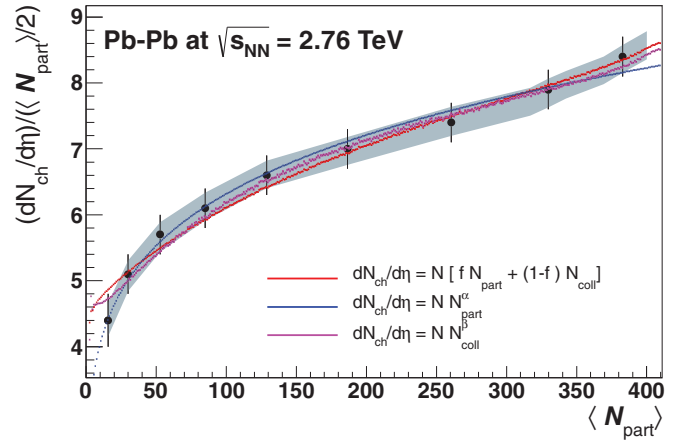

FIG. 11. (Color online) Centrality dependence of $dN_{\text{ch}}/d\eta$ per participant pair as a function of N_{part}, measured in the Pb-Pb data at $\sqrt{s_{NN}} = 2.76$ TeV fitted with various parametrizations of N_{part} and N_{coll}, calculated with the Glauber model. The fit parameters are given in the figure. Data are from Ref. [35].

The charged-particle multiplicity per participant pair $dN_{\text{ch}}/d\eta /(0.5 N_{\text{part}})$ measured by ALICE [35] is fitted (Fig. 11) with three different parametrizations of the ancestor dependence mentioned above:

(i) a two-components model: $dN_{\text{ch}}/d\eta \propto f N_{\text{part}} + (1 - f)N_{\text{coll}}$;
(ii) a power-law function of N_{part}: $dN_{\text{ch}}/d\eta \propto N_{\text{part}}^{\alpha}$;
(iii) a power-law function of N_{coll}: $dN_{\text{ch}}/d\eta \propto N_{\text{coll}}^{\beta}$;

and the fit parameters are reported in Table II. We note that the value obtained for f is in a good agreement with the value obtained in the NBD-Glauber fit, shown in Fig. 10.

While the value obtained for α and for β with the power-law parametrization of N_{part} and N_{coll} indicate that neither of these scalings perfectly describes the data ($\alpha > 1$ and $\beta < 1$), we note that the value of α is similar to that measured at RHIC (1.16 ± 0.04 [39]) and slightly higher than that at the SPS ($\alpha \sim 1$, see Ref. [36] for a review). The results obtained with the two-component model, where $0 < f < 1$, indicate that the contributions of both N_{part} and N_{coll} are needed to explain the particle production confirm this. However, the χ^2/NDF reported in Table II indicate an equally good fit for all models, thus revealing that no unique physics conclusion can be drawn from such fits and that the particular choice of parametrization has no influence on the results of the centrality determination.

TABLE II. Parameters of the fit to the charged-particle multiplicity for the three different parametrizations discussed in the text, with error and χ^2/NDF.

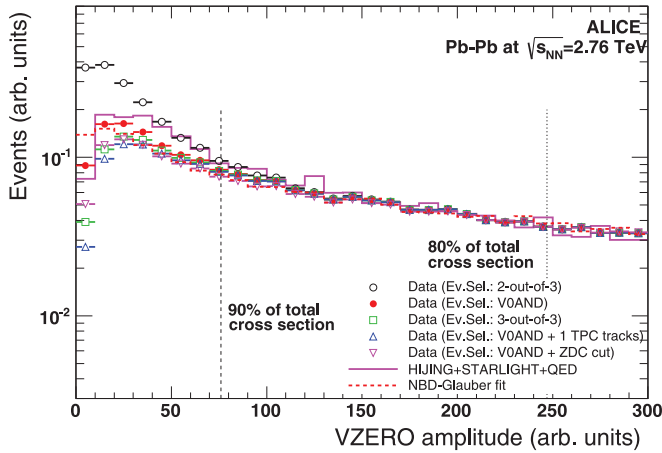| Model	Normalization	Error	Fit par.	Error	χ^2/NDF
$f N_{\text{part}}$ $+(1 - f)N_{\text{coll}}$	2.441	0.281	$f = 0.788$	0.021	0.347
N_{part}^{α}	1.317	0.116	$\alpha = 1.190$	0.017	0.182
N_{coll}^{β}	4.102	0.297	$\beta = 0.803$	0.012	0.225

FIG. 12. (Color online) Distribution of the VZERO amplitude zoomed in the most peripheral region. The distribution is compared to the NBD-Glauber fit and to the sum of the HIJING + STARLIGHT + QED simulations.

C. Systematic uncertainty on the anchor point

The determination of the AP by either correcting or fitting the multiplicity distribution is evaluated in Fig. 12 by comparing the VZERO amplitude distributions for various event selections. The systematic uncertainty on the AP is estimated by comparing the percentage of the hadronic cross section at the VZERO amplitude chosen as the AP (V0$_{AP}$) obtained correcting or fitting the multiplicity distribution. For the first method (Sec. IV A), we used the results from the HIJING and AMPT simulations. For the second method (Sec. IV B), we used alternative centrality definitions based on (i) TPC tracks; (ii) SPD hit multiplicities, and obtaining a value for the V0$_{AP}$ using the correlation between SPD or TPC and VZERO; (iii) different ranges for the Glauber model fit; (iv) different ancestor dependence of the particle production model to a power law of N_{part}; and (v) different nucleon-nucleon cross section and parameters of the Woods-Saxon distribution within their estimated uncertainties. All the results, compared in Table III, allow us to define the AP as the VZERO amplitude above which we obtain 90% of the hadronic cross section with the NBD-Glauber fit (the baseline in Table III) with a systematic uncertainty of 1%, determined as the rms of all the results presented in Table III. The variations of the AP are not part of the quoted systematic uncertainties for N_{part}, N_{coll}, and T_{AA}, which include only variations of the Glauber parameters. The uncertainty on the AP is typically included in our analyses as an uncertainty on the limits of the centrality classes and propagated into an uncertainty on the specific measured observable.

V. CENTRALITY CLASSES AND THEIR RELATION WITH GEOMETRICAL QUANTITIES

A. Determination of the centrality classes with the multiplicity distributions

The percentile of the hadronic cross section is determined for any value of the VZERO amplitude by integrating the measured VZERO amplitude distribution normalized at the

TABLE III. Comparison of the percentage of the hadronic cross section above the VZERO amplitude chosen as AP (V0$_{AP}$) for various cases considered in the systematic studies of the Glauber fits and with HIJING and AMPT simulations.

Method	% of total cross section above the V0$_{AP}$
Glauber Fits	
Baseline	90.00
(i) Fit TPC tracks	89.88
(ii) Fit SPD clusters	89.87
(iii) Fit only 50% of cross section	90.11
(iv) Different ancestor dependence	90.66
(v) Different Wood-Saxons par	90.43
HIJING simulations	
2-out-of-3	92.50
V0AND	89.05
3-out-of-3	90.15
V0AND + TPC	91.12
V0AND + ZDC	89.52
AMPT simulations	
2-out-of-3	92.49
V0AND	89.49
3-out-of-3	90.59
V0AND + TPC	91.36
V0AND + ZDC	89.00

anchor point V0$_{AP}$, i.e., 90% of the hadronic cross section. For example, if we define V as the VZERO amplitude, the top 10% central class is defined by the boundary V0$_{10}$ which satisfies

$$\frac{\int_{V0_{10}}^{\infty} (dN_{evt}/dV)\, dV}{\int_{V0_{AP}}^{\infty} (dN_{evt}/dV)\, dV} = \frac{1}{9}. \tag{6}$$

The same is done for the number of clusters in the SPD and the number of reconstructed tracks in the TPC. The events with multiplicity lower than that of the anchor point, contaminated by EM background and trigger inefficiency, are not used in the physics analyses.

One can divide the experimental distribution into classes by defining sharp cuts on, e.g., the VZERO amplitude, which correspond to well-defined percentile intervals of the hadronic cross section. The number of centrality classes that one can define is connected with the resolution achieved on the quantities used in the definition. In general, centrality classes are defined so the separation between the central values of b and N_{part} for two adjacent classes is significantly larger than the resolution of that variable (see Sec. VI).

B. Finding the number of participants with the multiplicity distributions

In Sec. IV B we fit the measured VZERO amplitude distribution with the amplitude distribution simulated with the NBD-Glauber. This creates a connection between an experimental observable and the geometrical model of nuclear collisions used in the Glauber Monte Carlo. From this we can access the geometrical properties, like N_{part}, N_{coll}, and T_{AA}. A given centrality class, defined by sharp cuts in the

TABLE IV. N_{part} for Pb-Pb collisions at $\sqrt{s_{NN}} = 2.76$ TeV with the corresponding uncertainties derived from a Glauber calculation. The $\langle N_{\text{part}}^{\text{data}} \rangle$ are calculated from the NBD-Glauber fit to the VZERO amplitude, while the $\langle N_{\text{part}}^{\text{geo}} \rangle$ are obtained by slicing the impact parameter distribution. $\langle N_{\text{part}}^{\text{data}} \rangle$ is also calculated for two variations of the AP, i.e., moving it to 91% ($\langle N_{\text{part}}^{\text{data+}} \rangle$) and to 89% ($\langle N_{\text{part}}^{\text{data+}} \rangle$), respectively. The last three columns report the discrepancies between $\langle N_{\text{part}}^{\text{geo}} \rangle$ and $\langle N_{\text{part}}^{\text{data}} \rangle$ and $\langle N_{\text{part}}^{\text{data}} \rangle$ with the uncertainty of the AP.

Centrality	$\langle N_{\text{part}}^{\text{geo}} \rangle$ (syst. %)	$\langle N_{\text{part}}^{\text{data}} \rangle$	rms	$\langle N_{\text{part}}^{\text{data+}} \rangle$	$\langle N_{\text{part}}^{\text{data-}} \rangle$	$\Delta_{\text{geo}}^{\text{data}}$ (%)	$\Delta_{\text{data}}^{\text{data+}}$ (%)	$\Delta_{\text{data}}^{\text{data-}}$ (%)
0–1%	403.8 (0.35)	400.8	7.8	400.8	400.7	0.38	0.0041	0.0066
1–2%	393.6 (0.46)	392.5	11	392.7	392.3	0.14	0.021	0.018
2–3%	382.9 (0.6)	382.9	12	383.2	382.6	0.00013	0.037	0.035
3–4%	372 (0.73)	372.2	13	372.7	371.8	0.033	0.057	0.062
4–5%	361.1 (0.83)	361.4	13	362	360.9	0.047	0.081	0.072
5–10%	329.4 (1.1)	329.7	20	330.5	328.8	0.047	0.12	0.13
10–15%	281.2 (1.4)	281.6	18	282.8	280.3	0.064	0.21	0.23
15–20%	239 (1.6)	239.5	17	241	237.9	0.099	0.31	0.32
20–25%	202.1 (1.8)	202.7	15	204.4	200.9	0.14	0.42	0.43
25–30%	169.5 (1.9)	170.1	14	171.9	168.2	0.17	0.53	0.56
30–35%	141 (2)	141.7	12	143.6	139.7	0.24	0.66	0.7
35–40%	116 (2.2)	116.7	11	118.6	114.7	0.31	0.81	0.86
40–45%	94.11 (2.1)	94.77	9.7	96.68	92.83	0.35	1	1
45–50%	75.3 (2.3)	75.91	8.4	77.72	74.02	0.4	1.2	1.3
50–55%	59.24 (2.5)	59.77	7.3	61.49	58.02	0.44	1.4	1.5
55–60%	45.58 (2.9)	46.1	6.3	47.66	44.47	0.57	1.7	1.8
60–65%	34.33 (2.6)	34.65	5.4	36.09	33.2	0.47	2	2.1
65–70%	25.21 (4)	25.38	4.5	26.62	24.16	0.34	2.4	2.5
70–75%	17.96 (3.3)	18.06	3.8	19.07	17	0.27	2.7	3
75–80%	12.58 (3.7)	12.45	3	13.25	11.61	0.54	3.1	3.5
80–85%	8.812 (2.8)	8.275	2.4	8.914	7.646	3.1	3.7	4
85–90%	6.158 (2.4)	5.516	1.8	6.035	3.406	5.5	4.5	24

measured distribution, corresponds to the same class in the simulated distribution. For the simulated distribution we retain the input information from the Glauber model. Therefore, we can calculate the mean number of participants $\langle N_{\text{part}} \rangle$, the mean number of collisions $\langle N_{\text{coll}} \rangle$, and the average nuclear overlap function $\langle T_{AA} \rangle$ for centrality classes defined by sharp cuts in the simulated multiplicity distribution, corresponding to given percentiles of the hadronic cross section. As shown in Table IV, the mean values and their dispersions differ from those calculated for geometrical classes, defined by sharp cuts in the impact parameter b (Table I), by less than 1% for the most central classes (up to about 50%) and by less than 2% for the most peripheral ones (above 50%). This confirms that multiplicity fluctuations and detector resolution only play a minor role in the centrality determination.

C. Determination of the centrality classes with the ZDC

Another way to determine the centrality is to measure the energy deposited by the spectators in the ZDC. The spectator neutrons and protons having a rapidity close to that of the beam are detected in the ZDC. Naively, measurement of the number of spectator neutrons and protons would give direct measurement of the number of participants since N_{part} would simply be given by

$$N_{\text{part}} = 2A - E_{\text{ZDC}}/E_{\text{A}}, \qquad (7)$$

where E_{ZDC} is the energy measured in the ZDC, $A = 208$ is the mass number of Pb, and E_{A} is the beam energy per nucleon. However, fragment formation among the spectator nucleons breaks the simple linear and monotonic relation in the measured variables, since some spectator nucleons are bound into light nuclear fragments that have a charge over mass ratio similar to the beam, therefore remaining inside the beam pipe and are undetected by the ZDC [42,43]. This effect becomes quantitatively important for peripheral events and, therefore, Eq. (7) cannot be used as a reliable estimate of N_{part}.

Consequently, the ZDC information needs to be correlated to another quantity that has a monotonic relation with N_{part}. In our case, we use the energy measured by two small EM calorimeters (ZEM). These detectors are placed only on the A side about 7.5 m from the interaction point, covering the region $4.8 < \eta < 5.7$ [10].

Since the ZDC calorimeters are far from the interaction region, and therefore have an acceptance insensitive to the vertex position, a centrality measurement based on the ZDC is particularly suited for any analysis that does not require a vertex cut [44].

Centrality classes are defined by cuts on the two-dimensional distribution of the ZDC energy as a function of the ZEM amplitude. The ZDC signal is proportional to N_{part} for central events, while the ZEM amplitude is an unknown function of N_{part} and N_{coll}. Therefore the definition of the centrality classes in this two-dimensional space is not trivial. As shown in Fig. 13, centrality classes are defined by using the centrality classes defined previously with the VZERO amplitude to determine regions in the ZDC-ZEM plane, corresponding to a given centrality. The boundaries
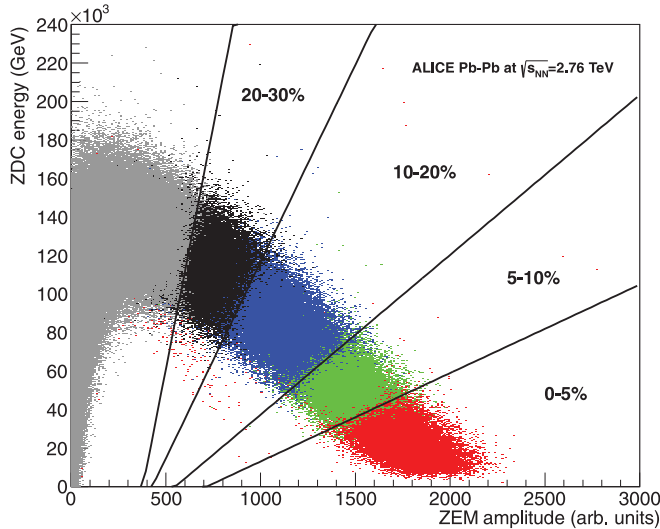
FIG. 13. (Color online) Spectator energy deposited in the ZDC calorimeters as a function of ZEM amplitude. The same correlation is shown for different centrality classes (5%, 10%, 20%, and 30%) obtained by selecting specific VZERO amplitudes. The lines are a fit to the boundaries of the centrality classes with linear functions, where only the slope is fitted and the offset point is fixed (see text).

between centrality classes, or the points belonging to the same narrow centrality class c ($c \pm \delta c$), can be fitted with linear functions. All these lines are found to intersect at a common point. Using this common point, we refitted the boundaries of the various centrality classes with the linear functions shown in Fig. 13.

As can be seen from the figure, the slopes of the fitted functions increase going from central to peripheral collisions and tend to infinity, as the lines become almost straight vertical lines, when approaching the point where the correlation between ZDC and ZEM inverts its sign. The value of the slope that defines a centrality class in the ZDC vs ZEM phase space is proportional to the tangent of the percentile, which implies that the percentiles behave like an angle in the ZDC vs ZEM phase space.

This function of ZDC and ZEM then can be used as centrality estimator for the most central events (0–30%) above the turning point of ZDC. Figure 14 shows the distribution of the VZERO amplitude for all triggered events and for various centrality classes selected with this method.

VI. RESOLUTION OF THE CENTRALITY DETERMINATION

As described above, two independent methods are used to determine experimentally the centrality of the collision. The first one uses the multiplicity distributions from various detectors covering different pseudorapidity ranges. Specifically, we use the sum of the amplitude in the VZERO detectors (A and C side), the number of clusters in the outer layer of the SPD detector, and the number of tracks reconstructed in the TPC. The second method uses the ZDC correlated with the ZEM.
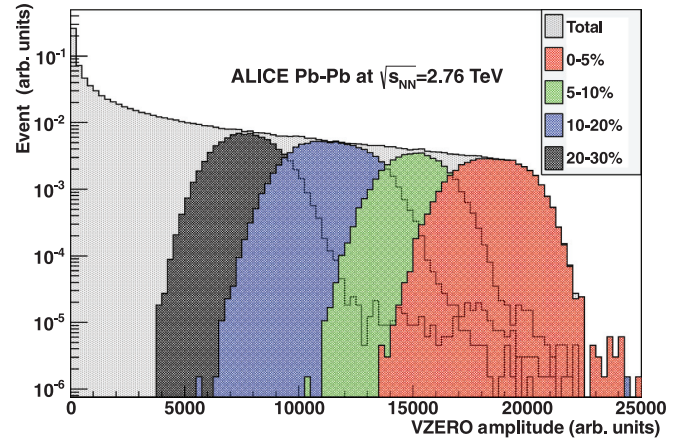

FIG. 14. (Color online) VZERO amplitude distribution of events of various centrality classes selected from the correlation between ZDC and ZEM amplitudes explained in the text.

The accuracy of the experimental determination of the centrality was evaluated by comparing the different estimates event by event. For example, in Fig. 15 we compare the estimates based on the SPD multiplicity and the VZERO amplitude. The VZERO amplitude distribution is shown for two centrality classes selected by the SPD multiplicity. The distributions for the two centrality classes are reasonably well fitted with a Gaussian distribution.

The resolution in the experimental definition of the centrality classes is evaluated event by event as the rms of the distribution of the differences between the centrality determined over all estimators and the mean value of the
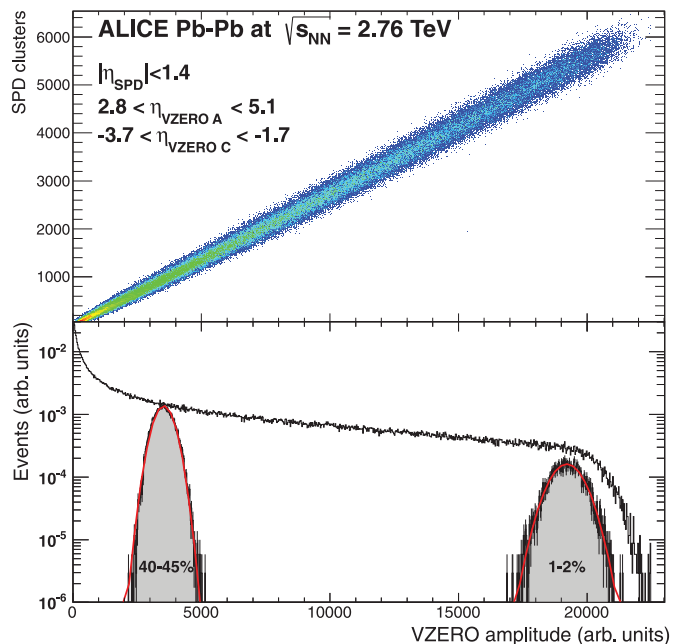

FIG. 15. (Color online) Top: Correlation between SPD multiplicity and VZERO amplitude. The rapidity coverage of each detector is indicated on the figure. Bottom: VZERO amplitude distributions for the centrality classes selected by SPD. Two centrality classes (1–2% and 40–45%) are indicated and fitted with a Gaussian.
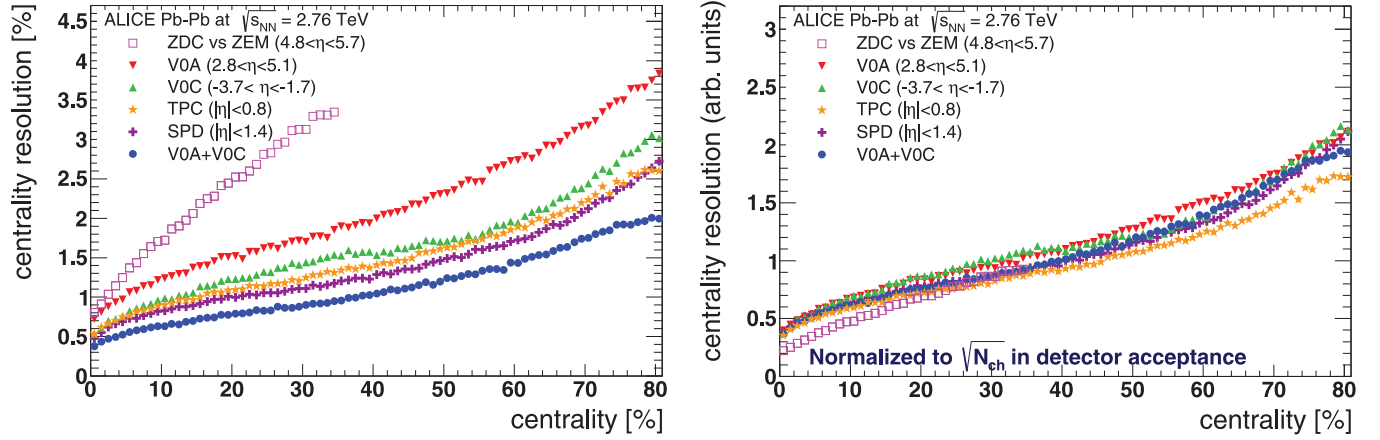
FIG. 16. (Color online) Left: Centrality resolution Δ_i for all the estimators evaluated in the analysis. Right: Resolution, in arbitrary units, scaled by $\sqrt{N_{ch}}$ measured in each detector.

centrality for the event. First, the average value of the centrality $\langle c \rangle$ is calculated for each event by averaging the centrality determined by each estimator,

$$\langle c \rangle = \frac{\sum_{i=0}^{N} c_i}{N}. \tag{8}$$

c_i is the centrality of an event determined by an estimator i, where i is the index running over all $N = 6$ centrality estimators used: VZERO (A and C), SPD, TPC, and ZDC. In the next step, the centrality is weighted by $\Delta_i = c_i - \langle c \rangle$: The difference between the centrality determined by each estimator and the mean value of the centrality from Eq. (8),

$$\langle c \rangle = \frac{\sum_{i=0}^{N} c_i / \Delta_i^2}{\sum_{i=0}^{N} 1 / \Delta_i^2}. \tag{9}$$

This latter calculation is performed iteratively replacing $\langle c \rangle$ by the new value until convergence is achieved which typically occurs after the second iteration. Finally, the centrality resolution of an estimator is evaluated as the rms of its Δ_i distribution for each centrality.

The ZDC-ZEM estimator is ignored for peripheral events ($\langle c \rangle > 35\%$) since its results are reliable only for the most central collisions. The resolution is shown in Fig. 16 (left panel) as a function of the centrality percentile.

The resolution depends on the rapidity coverage of the detector used. The best centrality resolution is achieved when combining the VZERO-A and VZERO-C detectors, due to the large pseudorapidity coverage (4.3 units in total). It ranges from 0.5% in central to 2% in peripheral collisions. The resolution obtained with the SPD and the TPC ranges from 1% in central to 3% in peripheral collisions ($\gtrsim 80\%$).

We measured the pseudorapidity dependence of the charged-particle multiplicity at midrapidity [45] with the SPD and at forward rapidity [46] using all the rapidity coverage of the SPD, the VZERO, and the FMD detectors. The total charged-particle multiplicity N_{ch} is obtained by integration. The centrality resolution was scaled by $\sqrt{N_{ch}}$ measured in the rapidity window of each detector (see right panel of Fig. 16). The figure shows that all the results are consistent on an arbitrary unit scale, except for the ZDC-ZEM estimator, which

is better for central collisions because it uses information from two detectors.

The centrality resolution was tested with a full HIJING and GEANT detector simulation. In the HIJING simulations the true value of the event centrality (c_{true}) is known for every given event. After using GEANT one obtains the signals in VZERO, SPD, and TPC for the given event and, hence, using these centrality estimators can calculate the value of the $\langle c \rangle$ for the given event with Eq. (8). The real centrality resolution, given for the given event by the difference between the c_{true} and the $\langle c \rangle$ calculated for each extimator, is consistent with the one calculated with data.

VII. SUMMARY

Heavy-ion collisions can be characterized by the number of charged particles produced in the collision. In principle, when normalized to the trigger efficiency used to collect the data sample, the charged-particle multiplicity could provide a measurement of the hadronic cross section. However, at the LHC the large cross section for EM processes contaminates the very peripheral collisions. This problem was overcome in two ways.

In the first method, dedicated simulations of hadronic and EM processes (Fig. 8) were performed and data were corrected for efficiency of the event selection (Fig. 7) and purity of the event sample (Fig. 9). In the second method, the measured multiplicity distribution was fitted with a Glauber calculation (Fig. 10). Both methods allow us to determine a centrality value above which the background contamination is negligible and the event selection is fully efficient. The corresponding value of multiplicity and centrality is defined as the anchor point and is used for the centrality normalization (Table III).

Using the AP, the measured event sample can be divided in centrality classes which correspond to well-defined percentiles of the hadronic cross section. Several approaches were developed. The first method uses charged-particle multiplicity (measured by various detectors, with different rapidity coverage, such as the VZERO, the SPD, and the TPC). The second

method uses the ZDC, which measures the nucleon spectators directly, as well as the correlation to the ZEM energy in order to resolve the ambiguity due to nuclear fragmentation. The centrality is obtained from linear functions that fit the contours of the classes defined by the VZERO, in the ZDC-ZEM plane (Fig. 13). As standard method, typically used in ALICE physics analyses, we used the NBD-Glauber fit to the VZERO amplitude (Fig. 10) to determine the AP, and the other methods described to asses a systematic uncertainty on the centrality determination.

The resolution of the centrality determination, which depends on the pseudorapidity coverage of the detector used, was determined as the weighed rms of all the estimates; it ranges from 0.5% in central to 2% in peripheral collisions (Fig. 16).

Finally, mean numbers of the relevant geometrical quantities, such as N_{part} and N_{coll}, were calculated for typical centrality classes, using the Glauber Model and the fit to the measured multiplicity distribution (Table I). This fit creates a mapping between a measured quantity and one obtained with a phenomenological calculation for which the geometrical properties are known. The results, nearly identical to those obtained for centrality classes defined by classifying the events according to their impact parameter, provide a general tool to compare ALICE measurements with those of other experiments, at different energies and with different colliding systems as well as theoretical calculations.

APPENDIX: TABLES

As described in Sec. II, for the physics in ALICE analyses the average values of N_{part}, N_{coll}, or T_{AA} for centrality classes defined by sharp cuts in the impact parameter distributions are used. These are reported in Table I. Therefore $\langle N_{part}\rangle$, $\langle N_{coll}\rangle$, and $\langle T_{AA}\rangle$ depend exclusively on the nuclear geometrical parameters and not on any measured quantity. Their uncertainty is calculated by varying the parameters of the Glauber calculations (i.e., the parameters of the Woods-Saxon and the hadronic cross section σ_{NN}^{inel}) by the known uncertainty. We label the $\langle N_{part}\rangle$ calculated with this procedure as $\langle N_{part}^{geo}\rangle$.

Another possibility, discussed in Sec. V B, is to define the average values of N_{part}, N_{coll}, or T_{AA} for centrality classes by sharp cuts in the fitted multiplicity distribution. Following this strategy, it is also possible to incorporate in the uncertainty, besides the uncertainties related to the Glauber calculation, those related to the measurement of the AP: the experimental region which is actually being used for the physics analyses, because it is free of background and the trigger efficiency is known. In this case, the AP can be varied by the uncertainty that was estimated ($90\% \pm 1\%$) and recalculate $\langle N_{part}\rangle$, $\langle N_{coll}\rangle$, and $\langle T_{AA}\rangle$ with these variations. The $\langle N_{part}\rangle$ calculated with this procedure is labled as $\langle N_{part}^{data}\rangle$. The variations for the AP are labeled $\langle N_{part}^{data+}\rangle$ and $\langle N_{part}^{data-}\rangle$, respectively.

In Table IV $\langle N_{part}^{geo}\rangle$ is compared to $\langle N_{part}^{data}\rangle$ for various centrality classes. The default values of $\langle N_{part}^{data}\rangle$ are compared to the values obtained by varying the AP. The discrepancies Δ

TABLE V. Same as Table IV for N_{coll}.

Centrality	$\langle N_{\text{coll}}^{\text{geo}}\rangle$ (syst. %)	$\langle N_{\text{coll}}^{\text{data}}\rangle$	rms	$\langle N_{\text{coll}}^{\text{data}+}\rangle$	$\langle N_{\text{coll}}^{\text{data}-}\rangle$	$\Delta_{\text{geo}}^{\text{data}}$ (%)	$\Delta_{\text{data}}^{\text{data}+}$ (%)	$\Delta_{\text{data}}^{\text{data}-}$ (%)
0–1%	1861 (8.2)	1863	83	1864	1863	0.059	0.016	0.018
1–2%	1766 (8.2)	1761	79	1762	1759	0.15	0.04	0.047
2–3%	1678 (8.2)	1678	79	1680	1676	0.0063	0.063	0.067
3–4%	1597 (8.3)	1596	78	1599	1592	0.039	0.096	0.1
4–5%	1520 (8.1)	1520	77	1524	1516	0.002	0.12	0.12
5–10%	1316 (8.2)	1316	110	1321	1310	0.0099	0.2	0.2
10–15%	1032 (8.2)	1034	95	1040	1027	0.083	0.32	0.34
15–20%	809.8 (8)	811.7	80	819.2	803.9	0.11	0.46	0.48
20-25%	629.6 (7.8)	631	68	639	622.9	0.11	0.63	0.65
25–30%	483.7 (7.5)	485.8	57	493.6	477.7	0.22	0.79	0.85
30–35%	366.7 (7.4)	368.4	49	375.9	360.7	0.23	1	1.1
35–40%	273.4 (7.4)	274.8	40	281.7	267.8	0.26	1.2	1.3
40–45%	199.4 (6.9)	200.7	33	206.8	194.5	0.32	1.5	1.6
45–50%	143.1 (6.6)	143.8	26	149	138.6	0.26	1.8	1.9
50–55%	100.1 (6.5)	100.6	20	104.9	96.22	0.25	2.1	2.2
55–60%	68.46 (6.2)	68.7	15	72.12	65.28	0.18	2.4	2.6
60-65%	45.79 (5.7)	45.79	12	48.47	43.12	0.0038	2.8	3
65–70%	29.92 (6.8)	29.66	8.3	31.68	27.73	0.43	3.3	3.4
70–75%	19.08 (5.7)	18.82	5.8	20.22	17.39	0.68	3.6	4
75–80%	12.07 (5.7)	11.62	4	12.61	10.63	1.9	4.1	4.4
80–85%	7.682 (5.1)	6.925	2.7	7.595	6.269	5.2	4.6	5
85–90%	4.904 (4.1)	4.148	1.8	4.651	2.257	8.4	5.7	30

are calculated as

$$\Delta = \frac{\left|\langle N_{\text{part}}^{\text{geo}}\rangle - \langle N_{\text{part}}^{\text{data}}\rangle\right|}{\left(\langle N_{\text{part}}^{\text{geo}}\rangle + \langle N_{\text{part}}^{\text{data}}\rangle\right)}. \tag{A1}$$

The same comparison is done in Tables V and VI for $\langle N_{\text{coll}}\rangle$ and $\langle T_{AA}\rangle$, respectively. Table VII gives the comparison for the three quantities but for bigger centrality classes.

TABLE VI. Same as Table IV for T_{AA}.

Centrality	$\langle T_{\text{AB}}^{\text{geo}}\rangle$ (syst. %)	$\langle T_{\text{AB}}^{\text{data}}\rangle$	rms	$\langle T_{\text{AB}}^{\text{data}+}\rangle$	$\langle T_{\text{AB}}^{\text{data}-}\rangle$	$\Delta_{\text{geo}}^{\text{data}}$ (%)	$\Delta_{\text{data}}^{\text{data}+}$ (%)	$\Delta_{\text{data}}^{\text{data}-}$ (%)
0–1%	29.08 (3.2)	29.11	1.3	29.12	29.1	0.056	0.016	0.018
1–2%	27.6 (3.2)	27.51	1.2	27.53	27.48	0.16	0.04	0.047
2–3%	26.22 (3.2)	26.22	1.2	26.25	26.19	0.0038	0.063	0.067
3–4%	24.95 (3.2)	24.93	1.2	24.98	24.88	0.032	0.096	0.1
4–5%	23.75 (3.2)	23.75	1.2	23.8	23.69	0.0019	0.12	0.12
5–10%	20.56 (3.3)	20.56	1.8	20.64	20.47	0.0036	0.2	0.2
10–15%	16.13 (3.6)	16.15	1.5	16.26	16.04	0.068	0.32	0.34
15–20%	12.65 (3.7)	12.68	1.2	12.8	12.56	0.13	0.46	0.48
20–25%	9.837 (3.7)	9.86	1.1	9.984	9.733	0.12	0.63	0.65
25–30%	7.558 (3.4)	7.591	0.9	7.713	7.463	0.22	0.79	0.85
30–35%	5.73 (3.3)	5.756	0.76	5.873	5.636	0.23	1	1.1
35–40%	4.272 (3.7)	4.294	0.63	4.402	4.184	0.26	1.2	1.3
40–45%	3.115 (3.9)	3.136	0.51	3.231	3.039	0.33	1.5	1.6
45–50%	2.235 (4.2)	2.248	0.41	2.328	2.165	0.28	1.8	1.9
50–55%	1.564 (4.7)	1.572	0.32	1.639	1.504	0.25	2.1	2.2
55–60%	1.07 (5.2)	1.073	0.24	1.127	1.02	0.16	2.4	2.6
60–65%	0.7154 (5)	0.7154	0.18	0.7573	0.6737	0.0007	2.8	3
65–70%	0.4674 (6.2)	0.4635	0.13	0.4949	0.4333	0.42	3.3	3.4
70–75%	0.2981 (6.4)	0.2941	0.091	0.3159	0.2717	0.68	3.6	4
75–80%	0.1885 (6.9)	0.1815	0.062	0.197	0.1661	1.9	4.1	4.4
80–85%	0.12 (6.5)	0.1082	0.042	0.1187	0.09795	5.2	4.6	5
85–90%	0.076 62 (5.9)	0.064 81	0.028	0.072 67	0.035 26	8.4	5.7	30

TABLE VII. Same as above with bigger centrality classes.

Centrality	$\langle N_{\mathrm{part}}^{\mathrm{geo}} \rangle$ (syst. %)	$\langle N_{\mathrm{part}}^{\mathrm{data}} \rangle$	rms	$\langle N_{\mathrm{part}}^{\mathrm{data}+} \rangle$	$\langle N_{\mathrm{part}}^{\mathrm{data}-} \rangle$	$\Delta_{\mathrm{geo}}^{\mathrm{data}}$ (%)	$\Delta_{\mathrm{data}}^{\mathrm{data}+}$ (%)	$\Delta_{\mathrm{data}}^{\mathrm{data}-}$ (%)
0–5%	382.7 (0.77)	382	17	382.3	381.7	0.096	0.04	0.038
5–10%	329.6 (1.3)	329.7	18	330.5	328.8	0.015	0.13	0.13
10–20%	260.1 (1.5)	260.5	27	261.9	259.1	0.079	0.26	0.27
20–40%	157.2 (2)	157.8	35	159.6	155.9	0.19	0.58	0.6
40–60%	68.56 (2.9)	69.13	22	70.89	67.35	0.42	1.3	1.3
60–80%	22.52 (3.4)	22.64	12	23.76	21.51	0.27	2.4	2.6
	$\langle N_{\mathrm{coll}}^{\mathrm{geo}} \rangle$ (syst. %)	$\langle N_{\mathrm{coll}}^{\mathrm{data}} \rangle$	rms	$\langle N_{\mathrm{coll}}^{\mathrm{data}+} \rangle$	$\langle N_{\mathrm{coll}}^{\mathrm{data}-} \rangle$	$\Delta_{\mathrm{geo}}^{\mathrm{data}}$ (%)	$\Delta_{\mathrm{data}}^{\mathrm{data}+}$ (%)	$\Delta_{\mathrm{data}}^{\mathrm{data}-}$ (%)
0–5%	1685 (11)	1684	1.4e + 02	1686	1681	0.044	0.065	0.067
5–10%	1316 (11)	1316	1.1e + 02	1321	1310	0.011	0.2	0.2
10–20%	921.2 (10)	922.7	1.4e + 02	929.8	915.3	0.079	0.39	0.4
20–40%	438.4 (9.7)	440	1.5e + 02	447.5	432.3	0.19	0.85	0.89
40–60%	127.7 (8.8)	128.4	59	133.2	123.7	0.29	1.8	1.9
60–80%	26.71 (7.3)	26.48	18	28.25	24.74	0.43	3.2	3.4
	$\langle T_{\mathrm{AB}}^{\mathrm{geo}} \rangle$ (syst. %)	$\langle T_{\mathrm{AB}}^{\mathrm{data}} \rangle$	rms	$\langle T_{\mathrm{AB}}^{\mathrm{data}+} \rangle$	$\langle T_{\mathrm{AB}}^{\mathrm{data}-} \rangle$	$\Delta_{\mathrm{geo}}^{\mathrm{data}}$ (%)	$\Delta_{\mathrm{data}}^{\mathrm{data}+}$ (%)	$\Delta_{\mathrm{data}}^{\mathrm{data}-}$ (%)
0–5%	26.32 (3.2)	26.31	2.2	26.34	26.27	0.028	0.066	0.066
5–10%	20.56 (3.3)	20.56	1.7	20.64	20.47	0.0051	0.2	0.2
10–20%	14.39 (3.1)	14.42	2.2	14.53	14.3	0.092	0.39	0.4
20–40%	6.85 (3.3)	6.876	2.3	6.993	6.754	0.19	0.85	0.89
40–60%	1.996 (4.9)	2.007	0.92	2.081	1.933	0.28	1.8	1.9
60–80%	0.4174 (6.3)	0.4137	0.29	0.4414	0.3865	0.44	3.2	3.4

[1] D. Schwarz, Ann. Phys. **12**, 220 (2003).
[2] M. Miller, K. Reygers, S. J. Sanders, and P. Steinberg, Ann. Rev. Nucl. Part. Sci. **57**, 205 (2007).
[3] R. J. Glauber, Phys. Rev. **100**, 242 (1955).
[4] R. J. Glauber, *Lectures in Theoretical Physics*, edited by W. E. Brittin and L. G. Dunham (Interscience, New York, 1959), Vol. 1, p. 315.
[5] R. Glauber, Nucl. Phys. A **774**, 3 (2006).
[6] R. Bruce *et al.*, Phys. Rev. ST Accel. Beams **12**, 071002 (2009).
[7] O. Djuvsland and J. Nystrand, arXiv:1011.4908.
[8] K. Hencken, Y. Kharlov, and S. Sadovsk, Alice Internal Note No. ALICE-INT-2002-27, 2003 (unpublished).
[9] B. Abelev *et al.* (ALICE Collaboration), Phys. Rev. Lett. **109**, 252302 (2012).
[10] K. Aamodt *et al.* (ALICE Collaboration), J. Instrum. **3**, S08002 (2008).
[11] D. D'Enterria and K. Reygers (private communication).
[12] K. Nakamura *et al.* (Particle Data Group), J. Phys. G **37**, 075021 (2010).
[13] M. Block, arXiv:1109.2940.
[14] J. Cudell *et al.* (COMPETE Collaboration), Phys. Rev. Lett. **89**, 201801 (2002).
[15] G. Aad *et al.* (ATLAS Collaboration), arXiv:1104.0326.
[16] Performance Analysis Note CMS-PASFWD-11-001 (2011) (unpublished).
[17] G. Antchev *et al.* (TOTEM Collaboration), arXiv:1110.1395.
[18] B. Abelev *et al.* (ALICE Collaboration), arXiv:1208.4968.
[19] A. P. T. W. Ludlam and A. Shor, BNL 51921 (1985).
[20] A. Shor and R. Longacre, Phys. Lett. B **218**, 100 (1989).
[21] B. Alver, M. Baker, C. Loizides, and P. Steinberg, arXiv:0805.4411.

[22] H. De Vries, C. W. De Jager, and C. De Vries, At. Data Nucl. Data Tables **36**, 495 (1987).
[23] M. Rybczynski and W. Broniowski, Phys. Rev. C **84**, 064913 (2011).
[24] W. Broniowski, P. Bozek, and M. Rybczynski, Phys. Rev. C **76**, 054905 (2007).
[25] W. Broniowski and M. Rybczynski, Phys. Rev. C **81**, 064909 (2010).
[26] G. Baur, K. Hencken, D. Trautmann, S. Sadovsky, and Y. Kharlov, Phys. Rep. **364**, 359 (2002).
[27] L. Evans and P. Bryant, J. Instrum. **3**, S08001 (2008).
[28] X.-N. Wang and M. Gyulassy, Phys. Rev. D **44**, 3501 (1991).
[29] R. Engel, Z. Phys. C **66**, 203 (1995).
[30] R. Brun *et al.*, CERN Program Library Long Write-up, W5013, GEANT Detector Description and Simulation Tool (1994).
[31] K. Aamodt *et al.* (ALICE Collaboration), Eur. Phys. J. C **65**, 111 (2010).
[32] K. Aamodt *et al.* (ALICE Collaboration), Eur. Phys. J. C **68**, 89 (2010).
[33] D. Kharzeev, E. Levin, and M. Nardi, Nucl. Phys. A **747**, 609 (2005).
[34] W. Deng, X. Wang, and R. Xu, arXiv:1008.1841.
[35] K. Aamodt *et al.* (ALICE Collaboration), Phys. Rev. Lett. **106**, 032301 (2011).
[36] M. C. Abreu *et al.* (NA50 Collaboration), Phys. Lett. B **530**, 43 (2002).
[37] M. M. Aggarwal *et al.* (WA98 Collaboration), Eur. Phys. J. C **18**, 651 (2001).
[38] F. Antinori *et al.* (NA57 and WA97 Collaborations), J. Phys. G **27**, 391 (2001).

[39] S. Adler *et al.* (PHENIX Collaboration), Phys. Rev. C **71**, 034908 (2005).

[40] G. Aad *et al.* (ATLAS Collaboration), Phys. Lett. B **710**, 363 (2012).

[41] S. Chatrchyan *et al.* (CMS Collaboration), J. High Energy Phys. 08 (2011) 141.

[42] M. Gallio *et al.* (ALICE Collaboration), CERN-LHCC-1999-05 (1999).

[43] C. Oppedisano, ALICE Internal Note No. 2002-08 (2001).

[44] E. Abbas *et al.* (ALICE Collaboration), Phys. Lett. B (2013), doi: 10.1016/j.physletb.2013.09.022.

[45] K. Aamodt *et al.* (ALICE Collaboration), Phys. Rev. Lett. **105**, 252301 (2010).

[46] A. Toia *et al.* (ALICE Collaboration), J. Phys. G **38**, 124007 (2011).

B. Abelev,[1] J. Adam,[2] D. Adamová,[3] A. M. Adare,[4] M. M. Aggarwal,[5] G. Aglieri Rinella,[6] M. Agnello,[7,8] A. G. Agocs,[9] A. Agostinelli,[10] Z. Ahammed,[11] N. Ahmad,[12] A. Ahmad Masoodi,[12] S. U. Ahn,[13] S. A. Ahn,[13] M. Ajaz,[14] A. Akindinov,[15] D. Aleksandrov,[16] B. Alessandro,[7] A. Alici,[17,18] A. Alkin,[19] E. Almaráz Aviña,[20] J. Alme,[21] T. Alt,[22] V. Altini,[23] S. Altinpinar,[24] I. Altsybeev,[25] C. Andrei,[26] A. Andronic,[27] V. Anguelov,[28] C. Anson,[30] T. Antičić,[31] F. Antinori,[32] P. Antonioli,[17] L. Aphecetche,[33] H. Appelshäuser,[34] N. Arbor,[35] S. Arcelli,[10] A. Arend,[34] N. Armesto,[36] R. Arnaldi,[7] T. Aronsson,[4] I. C. Arsene,[27] M. Arslandok,[34] A. Asryan,[25] A. Augustinus,[6] R. Averbeck,[27] T. C. Awes,[37] J. Äystö,[38] M. D. Azmi,[12,39] M. Bach,[22] A. Badalà,[40] Y. W. Baek,[41,42] R. Bailhache,[34] R. Bala,[43,7] A. Baldisseri,[44] F. Baltasar Dos Santos Pedrosa,[6] J. Bán,[45] R. C. Baral,[46] R. Barbera,[47] F. Barile,[23] G. G. Barnaföldi,[9] L. S. Barnby,[48] V. Barret,[41] J. Bartke,[49] M. Basile,[10] N. Bastid,[41] S. Basu,[11] B. Bathen,[29] G. Batigne,[33] B. Batyunya,[50] C. Baumann,[34] I. G. Bearden,[51] H. Beck,[34] N. K. Behera,[52] I. Belikov,[53] F. Bellini,[10] R. Bellwied,[54] E. Belmont-Moreno,[20] G. Bencedi,[9] S. Beole,[55] I. Berceanu,[26] A. Bercuci,[26] Y. Berdnikov,[56] D. Berenyi,[9] A. A. E. Bergognon,[33] D. Berzano,[55,7] L. Betev,[6] A. Bhasin,[43] A. K. Bhati,[5] J. Bhom,[57] L. Bianchi,[55] N. Bianchi,[58] J. Bielčík,[2] J. Bielčíková,[3] A. Bilandzic,[51] S. Bjelogrlic,[59] F. Blanco,[54] F. Blanco,[60] D. Blau,[16] C. Blume,[34] M. Boccioli,[6] S. Böttger,[61] A. Bogdanov,[62] H. Bøggild,[51] M. Bogolyubsky,[63] L. Boldizsár,[9] M. Bombara,[64] J. Book,[34] H. Borel,[44] A. Borissov,[65] F. Bossú,[39] M. Botje,[66] E. Botta,[55] E. Braidot,[67] P. Braun-Munzinger,[27] M. Bregant,[33] T. Breitner,[61] T. A. Broker,[34] T. A. Browning,[68] M. Broz,[69] R. Brun,[6] E. Bruna,[55,7] G. E. Bruno,[23] D. Budnikov,[70] H. Buesching,[34] S. Bufalino,[55,7] P. Buncic,[6] O. Busch,[28] Z. Buthelezi,[39] D. Caballero Orduna,[4] D. Caffarri,[71,32] X. Cai,[72] H. Caines,[4] E. Calvo Villar,[73] P. Camerini,[74] V. Canoa Roman,[75] G. Cara Romeo,[17] F. Carena,[6] W. Carena,[6] N. Carlin Filho,[76] F. Carminati,[6] A. Casanova Díaz,[58] J. Castillo Castellanos,[44] J. F. Castillo Hernandez,[27] E. A. R. Casula,[77] V. Catanescu,[26] C. Cavicchioli,[6] C. Ceballos Sanchez,[78] J. Cepila,[2] P. Cerello,[7] B. Chang,[38,79] S. Chapeland,[6] J. L. Charvet,[44] S. Chattopadhyay,[80] S. Chattopadhyay,[11] M. Cherney,[81] C. Cheshkov,[6,82] B. Cheynis,[82] V. Chibante Barroso,[6] D. D. Chinellato,[54] P. Chochula,[6] M. Chojnacki,[51] S. Choudhury,[11] P. Christakoglou,[66] C. H. Christensen,[51] P. Christiansen,[83] T. Chujo,[57] S. U. Chung,[84] C. Cicalo,[85] L. Cifarelli,[10,6,18] F. Cindolo,[17] J. Cleymans,[39] F. Colamaria,[23] D. Colella,[23] A. Collu,[77] G. Conesa Balbastre,[35] Z. Conesa del Valle,[6] M. E. Connors,[4] G. Contin,[74] J. G. Contreras,[75] T. M. Cormier,[65] Y. Corrales Morales,[55] P. Cortese,[86] I. Cortés Maldonado,[87] M. R. Cosentino,[67] F. Costa,[6] M. E. Cotallo,[60] E. Crescio,[75] P. Crochet,[41] E. Cruz Alaniz,[20] R. Cruz Albino,[75] E. Cuautle,[88] L. Cunqueiro,[58] A. Dainese,[71,32] A. Danu,[89] D. Das,[80] I. Das,[90] S. Das,[91] K. Das,[80] S. Dash,[52] A. Dash,[92] S. De,[11] G. O. V. de Barros,[76] A. De Caro,[93,18] G. de Cataldo,[94] J. de Cuveland,[22] A. De Falco,[77] D. De Gruttola,[18] H. Delagrange,[33] A. Deloff,[95] N. De Marco,[7] E. Dénes,[9] S. De Pasquale,[93] A. Deppman,[76] G. D Erasmo,[23] R. de Rooij,[59] M. A. Diaz Corchero,[60] D. Di Bari,[23] T. Dietel,[29] C. Di Giglio,[23] S. Di Liberto,[96] A. Di Mauro,[6] P. Di Nezza,[58] R. Divià,[6] Ø. Djuvsland,[24] A. Dobrin,[65,83] T. Dobrowolski,[95] B. Dönigus,[27] O. Dordic,[97] O. Driga,[33] A. K. Dubey,[11] A. Dubla,[59] L. Ducroux,[82] P. Dupieux,[41] A. K. Dutta Majumdar,[80] D. Elia,[94] D. Emschermann,[29] H. Engel,[61] B. Erazmus,[6,33] H. A. Erdal,[21] B. Espagnon,[90] M. Estienne,[33] S. Esumi,[57] D. Evans,[48] G. Eyyubova,[97] D. Fabris,[71,32] J. Faivre,[35] D. Falchieri,[10] A. Fantoni,[58] M. Fasel,[27,28] R. Fearick,[39] D. Fehlker,[24] L. Feldkamp,[29] D. Felea,[89] A. Feliciello,[7] B. Fenton-Olsen,[67] G. Feofilov,[25] A. Fernández Téllez,[87] A. Ferretti,[55] A. Festanti,[71] J. Figiel,[49] M. A. S. Figueredo,[76] S. Filchagin,[70] D. Finogeev,[98] F. M. Fionda,[23] E. M. Fiore,[23] E. Floratos,[99] M. Floris,[6] S. Foertsch,[39] P. Foka,[27] S. Fokin,[16] E. Fragiacomo,[100] A. Francescon,[6,71] U. Frankenfeld,[27] U. Fuchs,[6] C. Furget,[35] M. Fusco Girard,[93] J. J. Gaardhøje,[51] M. Gagliardi,[55] A. Gago,[73] M. Gallio,[55] D. R. Gangadharan,[30] P. Ganoti,[37] C. Garabatos,[27] E. Garcia-Solis,[101] C. Gargiulo,[6] I. Garishvili,[1] J. Gerhard,[22] M. Germain,[33] C. Geuna,[44] A. Gheata,[6] M. Gheata,[89,6] B. Ghidini,[23] P. Ghosh,[11] P. Gianotti,[58] M. R. Girard,[102] P. Giubellino,[6] E. Gladysz-Dziadus,[49] P. Glässel,[28] R. Gomez,[103,75] E. G. Ferreiro,[36] L. H. González-Trueba,[20] P. González-Zamora,[60] S. Gorbunov,[22] A. Goswami,[104] S. Gotovac,[105] L. K. Graczykowski,[102] R. Grajcarek,[28] A. Grelli,[59] A. Grigoras,[6] C. Grigoras,[6] V. Grigoriev,[62] A. Grigoryan,[106] S. Grigoryan,[50] B. Grinyov,[19] N. Grion,[100] P. Gros,[83] J. F. Grosse-Oetringhaus,[6] J.-Y. Grossiord,[82] R. Grosso,[6] F. Guber,[98] R. Guernane,[35] B. Guerzoni,[10] M. Guilbaud,[82] K. Gulbrandsen,[51] H. Gulkanyan,[106] T. Gunji,[107] R. Gupta,[43] A. Gupta,[43] R. Haake,[29] Ø. Haaland,[24] C. Hadjidakis,[90] M. Haiduc,[89] H. Hamagaki,[107] G. Hamar,[9] B. H. Han,[108] L. D. Hanratty,[48] A. Hansen,[51] Z. Harmanová-Tóthová,[64] J. W. Harris,[4] M. Hartig,[34] A. Harton,[101] D. Hatzifotiadou,[17] S. Hayashi,[107] A. Hayrapetyan,[6,106] S. T. Heckel,[34] M. Heide,[29] H. Helstrup,[21] A. Herghelegiu,[26] G. Herrera Corral,[75] N. Herrmann,[28] B. A. Hess,[109] K. F. Hetland,[21] B. Hicks,[4] B. Hippolyte,[53] Y. Hori,[107] P. Hristov,[6] I. Hřivnáčová,[90] M. Huang,[24] T. J. Humanic,[30] D. S. Hwang,[108] R. Ichou,[41] R. Ilkaev,[70] I. Ilkiv,[95]

M. Inaba,[57] E. Incani,[77] G. M. Innocenti,[55] P. G. Innocenti,[6] M. Ippolitov,[16] M. Irfan,[12] C. Ivan,[27] M. Ivanov,[27] V. Ivanov,[56] A. Ivanov,[25] O. Ivanytskyi,[19] A. Jachołkowski,[47] P. M. Jacobs,[67] H. J. Jang,[13] R. Janik,[69] M. A. Janik,[102] P. H. S. Y. Jayarathna,[54] S. Jena,[52] D. M. Jha,[65] R. T. Jimenez Bustamante,[88] P. G. Jones,[48] H. Jung,[42] A. Jusko,[48] A. B. Kaidalov,[15] S. Kalcher,[22] P. Kaliňák,[45] T. Kalliokoski,[38] A. Kalweit,[110,6] J. H. Kang,[79] V. Kaplin,[62] A. Karasu Uysal,[6,111,112] O. Karavichev,[98] T. Karavicheva,[98] E. Karpechev,[98] A. Kazantsev,[16] U. Kebschull,[61] R. Keidel,[113] S. A. Khan,[11] K. H. Khan,[14] P. Khan,[80] M. M. Khan,[12] A. Khanzadeev,[56] Y. Kharlov,[63] B. Kileng,[21] M. Kim,[42] M. Kim,[79] S. Kim,[108] D. J. Kim,[38] B. Kim,[79] J. H. Kim,[108] J. S. Kim,[42] T. Kim,[79] D. W. Kim,[42,13] S. Kirsch,[22] I. Kisel,[22] S. Kiselev,[15] A. Kisiel,[102] J. L. Klay,[114] J. Klein,[28] C. Klein-Bösing,[29] M. Kliemant,[34] A. Kluge,[6] M. L. Knichel,[27] A. G. Knospe,[115] M. K. Köhler,[27] T. Kollegger,[22] A. Kolojvari,[25] M. Kompaniets,[25] V. Kondratiev,[25] N. Kondratyeva,[62] A. Konevskikh,[98] V. Kovalenko,[25] M. Kowalski,[49] S. Kox,[35] G. Koyithatta Meethaleveedu,[52] J. Kral,[38] I. Králik,[45] F. Kramer,[34] A. Kravčáková,[64] T. Krawutschke,[28] M. Krelina,[2] M. Kretz,[22] M. Krivda,[48,45] F. Krizek,[38] M. Krus,[2] E. Kryshen,[56] M. Krzewicki,[27] Y. Kucheriaev,[16] T. Kugathasan,[6] C. Kuhn,[53] P. G. Kuijer,[66] I. Kulakov,[34] J. Kumar,[52] P. Kurashvili,[95] A. Kurepin,[98] A. B. Kurepin,[98] A. Kuryakin,[70] S. Kushpil,[3] V. Kushpil,[3] H. Kvaerno,[97] M. J. Kweon,[28] Y. Kwon,[79] P. Ladrón de Guevara,[88] I. Lakomov,[90] R. Langoy,[24] S. L. La Pointe,[59] C. Lara,[61] A. Lardeux,[33] P. La Rocca,[47] R. Lea,[74] M. Lechman,[6] G. R. Lee,[48] K. S. Lee,[42] S. C. Lee,[42] I. Legrand,[6] J. Lehnert,[34] M. Lenhardt,[27] V. Lenti,[94] H. León,[20] I. León Monzón,[103] H. León Vargas,[34] P. Lévai,[9] S. Li,[72] J. Lien,[24] R. Lietava,[48] S. Lindal,[97] V. Lindenstruth,[22] C. Lippmann,[27,6] M. A. Lisa,[30] H. M. Ljunggren,[83] D. F. Lodato,[59] P. I. Loenne,[24] V. R. Loggins,[65] V. Loginov,[62] D. Lohner,[28] C. Loizides,[67] K. K. Loo,[38] X. Lopez,[41] E. López Torres,[78] G. Løvhøiden,[97] X.-G. Lu,[28] P. Luettig,[34] M. Lunardon,[71] J. Luo,[72] G. Luparello,[59] C. Luzzi,[6] R. Ma,[4] K. Ma,[72] D. M. Madagodahettige-Don,[54] A. Maevskaya,[98] M. Mager,[110,6] D. P. Mahapatra,[46] A. Maire,[28] M. Malaev,[56] I. Maldonado Cervantes,[88] L. Malinina,[50,116] D. Mal'Kevich,[15] P. Malzacher,[27] A. Mamonov,[70] L. Manceau,[7] L. Mangotra,[43] V. Manko,[16] F. Manso,[41] V. Manzari,[94] Y. Mao,[72] M. Marchisone,[41,55] J. Mareš,[117] G. V. Margagliotti,[74,100] A. Margotti,[17] A. Marín,[27] C. Markert,[115] M. Marquard,[34] I. Martashvili,[118] N. A. Martin,[27] P. Martinengo,[6] M. I. Martínez,[87] A. Martínez Davalos,[20] G. Martínez García,[33] Y. Martynov,[19] A. Mas,[33] S. Masciocchi,[27] M. Masera,[55] A. Masoni,[85] L. Massacrier,[33] A. Mastroserio,[23] A. Matyja,[49] C. Mayer,[49] J. Mazer,[118] M. A. Mazzoni,[96] F. Meddi,[119] A. Menchaca-Rocha,[20] J. Mercado Pérez,[28] M. Meres,[69] Y. Miake,[57] K. Mikhaylov,[50,45,15] L. Milano,[55] J. Milosevic,[97,120] A. Mischke,[59] A. N. Mishra,[104,121] D. Miśkowiec,[27] C. Mitu,[89] S. Mizuno,[57] J. Mlynarz,[65] B. Mohanty,[11,122] L. Molnar,[9,53] L. Montaño Zetina,[75] M. Monteno,[7] E. Montes,[60] T. Moon,[79] M. Morando,[71] D. A. Moreira De Godoy,[76] S. Moretto,[71] A. Morreale,[38] A. Morsch,[6] V. Muccifora,[58] E. Mudnic,[105] S. Muhuri,[11] M. Mukherjee,[11] H. Müller,[6] M. G. Munhoz,[76] S. Murray,[39] L. Musa,[6] J. Musinsky,[45] B. K. Nandi,[52] R. Nania,[17] E. Nappi,[94] C. Nattrass,[118] T. K. Nayak,[11] S. Nazarenko,[70] A. Nedosekin,[15] M. Nicassio,[23,27] M. Niculescu,[89,6] B. S. Nielsen,[51] T. Niida,[57] S. Nikolaev,[16] V. Nikolic,[31] S. Nikulin,[16] V. Nikulin,[56] B. S. Nilsen,[81] M. S. Nilsson,[97] F. Noferini,[17,18] P. Nomokonov,[50] G. Nooren,[59] A. Nyanin,[16] A. Nyatha,[52] C. Nygaard,[51] J. Nystrand,[24] A. Ochirov,[25] H. Oeschler,[110,6] S. Oh,[4] S. K. Oh,[42] J. Oleniacz,[102] A. C. Oliveira Da Silva,[76] C. Oppedisano,[7] A. Ortiz Velasquez,[83,88] A. Oskarsson,[83] P. Ostrowski,[102] J. Otwinowski,[27] K. Oyama,[28] K. Ozawa,[107] Y. Pachmayer,[28] M. Pachr,[2] F. Padilla,[55] P. Pagano,[93] G. Paić,[88] F. Painke,[22] C. Pajares,[36] S. K. Pal,[11] A. Palaha,[48] A. Palmeri,[40] V. Papikyan,[106] G. S. Pappalardo,[40] W. J. Park,[27] A. Passfeld,[29] B. Pastirčák,[45] D. I. Patalakha,[63] V. Paticchio,[94] B. Paul,[80] A. Pavlinov,[65] T. Pawlak,[102] T. Peitzmann,[59] H. Pereira Da Costa,[44] E. Pereira De Oliveira Filho,[76] D. Peresunko,[16] C. E. Pérez Lara,[66] D. Perrino,[23] W. Peryt,[102] A. Pesci,[17] V. Peskov,[6] Y. Pestov,[123] V. Petráček,[2] M. Petran,[2] M. Petris,[26] P. Petrov,[48] M. Petrovici,[26] C. Petta,[47] S. Piano,[100] M. Pikna,[69] P. Pillot,[33] O. Pinazza,[6] L. Pinsky,[54] N. Pitz,[34] D. B. Piyarathna,[54] M. Planinic,[31] M. Płoskoń,[67] J. Pluta,[102] T. Pocheptsov,[50] S. Pochybova,[9] P. L. M. Podesta-Lerma,[103] M. G. Poghosyan,[6] K. Polák,[117] B. Polichtchouk,[63] N. Poljak,[59] A. Pop,[26] S. Porteboeuf-Houssais,[41] V. Pospíšil,[2] B. Potukuchi,[43] S. K. Prasad,[65] R. Preghenella,[17,18] F. Prino,[7] C. A. Pruneau,[65] I. Pshenichnov,[98] G. Puddu,[77] V. Punin,[70] M. Putiš,[64] J. Putschke,[65] H. Qvigstad,[97] A. Rachevski,[100] A. Rademakers,[6] T. S. Räihä,[38] J. Rak,[38] A. Rakotozafindrabe,[44] L. Ramello,[86] A. Ramírez Reyes,[75] S. Raniwala,[104] R. Raniwala,[104] S. S. Räsänen,[38] B. T. Rascanu,[34] D. Rathee,[5] K. F. Read,[118] J. S. Real,[35] K. Redlich,[95,124] R. J. Reed,[4] A. Rehman,[24] P. Reichelt,[34] M. Reicher,[59] R. Renfordt,[34] A. R. Reolon,[58] A. Reshetin,[98] F. Rettig,[22] J.-P. Revol,[6] K. Reygers,[28] L. Riccati,[7] R. A. Ricci,[125] T. Richert,[83] M. Richter,[97] P. Riedler,[6] W. Riegler,[6] F. Riggi,[47,40] M. Rodríguez Cahuantzi,[87] A. Rodriguez Manso,[66] K. Røed,[24,97] E. Rogochaya,[50] D. Rohr,[22] D. Röhrich,[24] R. Romita,[27,126] F. Ronchetti,[58] P. Rosnet,[41] S. Rossegger,[6] A. Rossi,[6,71] C. Roy,[53] P. Roy,[80] A. J. Rubio Montero,[60] R. Rui,[74] R. Russo,[55] E. Ryabinkin,[16] A. Rybicki,[49] S. Sadovsky,[63] K. Šafařík,[6] R. Sahoo,[121] P. K. Sahu,[46] J. Saini,[11] H. Sakaguchi,[127] S. Sakai,[67] D. Sakata,[57] C. A. Salgado,[36] J. Salzwedel,[30] S. Sambyal,[43] V. Samsonov,[56] X. Sanchez Castro,[53] L. Šándor,[45] A. Sandoval,[20] M. Sano,[57] G. Santagati,[47] R. Santoro,[6,18] J. Sarkamo,[38] E. Scapparone,[17] F. Scarlassara,[71] R. P. Scharenberg,[68] C. Schiaua,[26] R. Schicker,[28] C. Schmidt,[27] H. R. Schmidt,[109] S. Schuchmann,[34] J. Schukraft,[6] T. Schuster,[4] Y. Schutz,[6,33] K. Schwarz,[27] K. Schweda,[27] G. Scioli,[10] E. Scomparin,[7] P. A. Scott,[48] R. Scott,[118] G. Segato,[71] I. Selyuzhenkov,[27] S. Senyukov,[53] J. Seo,[84] S. Serci,[77] E. Serradilla,[60,20] A. Sevcenco,[89] A. Shabetai,[33] G. Shabratova,[50] R. Shahoyan,[6] N. Sharma,[5,118] S. Sharma,[43] S. Rohni,[43] K. Shigaki,[127] K. Shtejer,[78] Y. Sibiriak,[16] E. Sicking,[29] S. Siddhanta,[85] T. Siemiarczuk,[95] D. Silvermyr,[37] C. Silvestre,[35] G. Simatovic,[88,31] G. Simonetti,[6] R. Singaraju,[11] R. Singh,[43] S. Singha,[11,122] V. Singhal,[11] T. Sinha,[80] B. C. Sinha,[11] B. Sitar,[69] M. Sitta,[86] T. B. Skaali,[97] K. Skjerdal,[24] R. Smakal,[2] N. Smirnov,[4] R. J. M. Snellings,[59] C. Søgaard,[83] R. Soltz,[1] H. Son,[108] J. Song,[84] M. Song,[79] C. Soos,[6] F. Soramel,[71] I. Sputowska,[49] M. Spyropoulou-Stassinaki,[99] B. K. Srivastava,[68] J. Stachel,[28] I. Stan,[89] G. Stefanek,[95]

M. Steinpreis,[30] E. Stenlund,[83] G. Steyn,[39] J. H. Stiller,[28] D. Stocco,[33] M. Stolpovskiy,[63] P. Strmen,[69] A. A. P. Suaide,[76] M. A. Subieta Vásquez,[55] T. Sugitate,[127] C. Suire,[90] R. Sultanov,[15] M. Šumbera,[3] T. Susa,[31] T. J. M. Symons,[67] A. Szanto de Toledo,[76] I. Szarka,[69] A. Szczepankiewicz,[49,6] M. Szymański,[102] J. Takahashi,[92] M. A. Tangaro,[23] J. D. Tapia Takaki,[90] A. Tarantola Peloni,[34] A. Tarazona Martinez,[6] A. Tauro,[6] G. Tejeda Muñoz,[87] A. Telesca,[6] A. Ter Minasyan,[16] C. Terrevoli,[23] J. Thäder,[27] D. Thomas,[59] R. Tieulent,[82] A. R. Timmins,[54] D. Tlusty,[2] A. Toia,[22,71,32] H. Torii,[107] L. Toscano,[7] V. Trubnikov,[19] D. Truesdale,[30] W. H. Trzaska,[38] T. Tsuji,[107] A. Tumkin,[70] R. Turrisi,[32] T. S. Tveter,[97] J. Ulery,[34] K. Ullaland,[24] J. Ulrich,[128,61] A. Uras,[82] G. M. Urciuoli,[96] G. L. Usai,[77] M. Vajzer,[2,3] M. Vala,[50,45] L. Valencia Palomo,[90] P. Vande Vyvre,[6] M. van Leeuwen,[59] L. Vannucci,[125] A. Vargas,[87] R. Varma,[52] M. Vasileiou,[99] A. Vasiliev,[16] V. Vechernin,[25] M. Veldhoen,[59] M. Venaruzzo,[74] E. Vercellin,[55] S. Vergara,[87] R. Vernet,[129] M. Verweij,[59] L. Vickovic,[105] G. Viesti,[71] J. Viinikainen,[38] Z. Vilakazi,[39] O. Villalobos Baillie,[48] L. Vinogradov,[25] A. Vinogradov,[16] Y. Vinogradov,[70] T. Virgili,[93] Y. P. Viyogi,[11] A. Vodopyanov,[50] M. A. Völkl,[28] K. Voloshin,[15] S. Voloshin,[65] G. Volpe,[6] B. von Haller,[6] I. Vorobyev,[25] D. Vranic,[27] J. Vrláková,[64] B. Vulpescu,[41] A. Vyushin,[70] B. Wagner,[24] V. Wagner,[2] R. Wan,[72] Y. Wang,[72] M. Wang,[72] D. Wang,[72] Y. Wang,[28] K. Watanabe,[57] M. Weber,[54] J. P. Wessels,[6,29] U. Westerhoff,[29] J. Wiechula,[109] J. Wikne,[97] M. Wilde,[29] A. Wilk,[29] G. Wilk,[95] M. C. S. Williams,[17] B. Windelband,[28] L. Xaplanteris Karampatsos,[115] C. G. Yaldo,[65] Y. Yamaguchi,[107] H. Yang,[44,59] S. Yang,[24] S. Yasnopolskiy,[16] J. Yi,[84] Z. Yin,[72] I.-K. Yoo,[84] J. Yoon,[79] W. Yu,[34] X. Yuan,[72] I. Yushmanov,[16] V. Zaccolo,[51] C. Zach,[2] C. Zampolli,[17] S. Zaporozhets,[50] A. Zarochentsev,[25] P. Závada,[117] N. Zaviyalov,[70] H. Zbroszczyk,[102] P. Zelnicek,[61] I. S. Zgura,[89] M. Zhalov,[56] X. Zhang,[67,41,72] H. Zhang,[72] Y. Zhou,[59] F. Zhou,[72] D. Zhou,[72] X. Zhu,[72] J. Zhu,[72] H. Zhu,[72] J. Zhu,[72] A. Zichichi,[10,18] A. Zimmermann,[28] G. Zinovjev,[19] Y. Zoccarato,[82] M. Zynovyev,[19] and M. Zyzak[34]

(ALICE Collaboration)

[1]*Lawrence Livermore National Laboratory, Livermore, California, USA*
[2]*Faculty of Nuclear Sciences and Physical Engineering, Czech Technical University in Prague, Prague, Czech Republic*
[3]*Nuclear Physics Institute, Academy of Sciences of the Czech Republic, Řež u Prahy, Czech Republic*
[4]*Yale University, New Haven, Connecticut, USA*
[5]*Physics Department, Panjab University, Chandigarh, India*
[6]*European Organization for Nuclear Research (CERN), Geneva, Switzerland*
[7]*Sezione INFN, Turin, Italy*
[8]*Politecnico di Torino, Turin, Italy*
[9]*Wigner Research Centre for Physics, Hungarian Academy of Sciences, Budapest, Hungary*
[10]*Dipartimento di Fisica e Astronomia dell'Università and Sezione INFN, Bologna, Italy*
[11]*Variable Energy Cyclotron Centre, Kolkata, India*
[12]*Department of Physics, Aligarh Muslim University, Aligarh, India*
[13]*Korea Institute of Science and Technology Information, Daejeon, South Korea*
[14]*COMSATS Institute of Information Technology (CIIT), Islamabad, Pakistan*
[15]*Institute for Theoretical and Experimental Physics, Moscow, Russia*
[16]*Russian Research Centre Kurchatov Institute, Moscow, Russia*
[17]*Sezione INFN, Bologna, Italy*
[18]*Centro Fermi, Museo Storico della Fisica e Centro Studi e Ricerche "Enrico Fermi," Rome, Italy*
[19]*Bogolyubov Institute for Theoretical Physics, Kiev, Ukraine*
[20]*Instituto de Física, Universidad Nacional Autónoma de México, Mexico City, Mexico*
[21]*Faculty of Engineering, Bergen University College, Bergen, Norway*
[22]*Frankfurt Institute for Advanced Studies, Johann Wolfgang Goethe–Universität Frankfurt, Frankfurt, Germany*
[23]*Dipartimento Interateneo di Fisica "M. Merlin" and Sezione INFN, Bari, Italy*
[24]*Department of Physics and Technology, University of Bergen, Bergen, Norway*
[25]*V. Fock Institute for Physics, St. Petersburg State University, St. Petersburg, Russia*
[26]*National Institute for Physics and Nuclear Engineering, Bucharest, Romania*
[27]*Research Division and ExtreMe Matter Institute EMMI, GSI Helmholtzzentrum für Schwerionenforschung, Darmstadt, Germany*
[28]*Physikalisches Institut, Ruprecht-Karls-Universität Heidelberg, Heidelberg, Germany*
[29]*Institut für Kernphysik, Westfälische Wilhelms-Universität Münster, Münster, Germany*
[30]*Department of Physics, Ohio State University, Columbus, Ohio, USA*
[31]*Rudjer Bošković Institute, Zagreb, Croatia*
[32]*Sezione INFN, Padova, Italy*
[33]*SUBATECH, Ecole des Mines de Nantes, Université de Nantes, CNRS-IN2P3, Nantes, France*
[34]*Institut für Kernphysik, Johann Wolfgang Goethe-Universität Frankfurt, Frankfurt, Germany*
[35]*Laboratoire de Physique Subatomique et de Cosmologie (LPSC), Université Joseph Fourier,*
CNRS-IN2P3, Institut Polytechnique de Grenoble, Grenoble, France

[36]*Departamento de Física de Partículas and IGFAE, Universidad de Santiago de Compostela, Santiago de Compostela, Spain*
[37]*Oak Ridge National Laboratory, Oak Ridge, Tennessee, USA*
[38]*Helsinki Institute of Physics (HIP) and University of Jyväskylä, Jyväskylä, Finland*
[39]*Physics Department, University of Cape Town and iThemba LABS, National Research Foundation, Somerset West, South Africa*
[40]*Sezione INFN, Catania, Italy*
[41]*Laboratoire de Physique Corpusculaire (LPC), Clermont Université, Université Blaise Pascal, CNRS–IN2P3, Clermont-Ferrand, France*
[42]*Gangneung-Wonju National University, Gangneung, South Korea*
[43]*Physics Department, University of Jammu, Jammu, India*
[44]*Commissariat à l'Energie Atomique, IRFU, Saclay, France*
[45]*Institute of Experimental Physics, Slovak Academy of Sciences, Košice, Slovakia*
[46]*Institute of Physics, Bhubaneswar, India*
[47]*Dipartimento di Fisica e Astronomia dell'Università and Sezione INFN, Catania, Italy*
[48]*School of Physics and Astronomy, University of Birmingham, Birmingham, United Kingdom*
[49]*The Henryk Niewodniczanski Institute of Nuclear Physics, Polish Academy of Sciences, Cracow, Poland*
[50]*Joint Institute for Nuclear Research (JINR), Dubna, Russia*
[51]*Niels Bohr Institute, University of Copenhagen, Copenhagen, Denmark*
[52]*Indian Institute of Technology Bombay (IIT), Mumbai, India*
[53]*Institut Pluridisciplinaire Hubert Curien (IPHC), Université de Strasbourg, CNRS-IN2P3, Strasbourg, France*
[54]*University of Houston, Houston, Texas, USA*
[55]*Dipartimento di Fisica dell'Università and Sezione INFN, Turin, Italy*
[56]*Petersburg Nuclear Physics Institute, Gatchina, Russia*
[57]*University of Tsukuba, Tsukuba, Japan*
[58]*Laboratori Nazionali di Frascati, INFN, Frascati, Italy*
[59]*Nikhef, National Institute for Subatomic Physics and Institute for Subatomic Physics of Utrecht University, Utrecht, Netherlands*
[60]*Centro de Investigaciones Energéticas Medioambientales y Tecnológicas (CIEMAT), Madrid, Spain*
[61]*Institut für Informatik, Johann Wolfgang Goethe-Universität Frankfurt, Frankfurt, Germany*
[62]*Moscow Engineering Physics Institute, Moscow, Russia*
[63]*Institute for High Energy Physics, Protvino, Russia*
[64]*Faculty of Science, P. J. Šafárik University, Košice, Slovakia*
[65]*Wayne State University, Detroit, Michigan, USA*
[66]*Nikhef, National Institute for Subatomic Physics, Amsterdam, Netherlands*
[67]*Lawrence Berkeley National Laboratory, Berkeley, California, USA*
[68]*Purdue University, West Lafayette, Indiana, USA*
[69]*Faculty of Mathematics, Physics and Informatics, Comenius University, Bratislava, Slovakia*
[70]*Russian Federal Nuclear Center (VNIIEF), Sarov, Russia*
[71]*Dipartimento di Fisica e Astronomia dell'Università and Sezione INFN, Padova, Italy*
[72]*Central China Normal University, Wuhan, China*
[73]*Sección Física, Departamento de Ciencias, Pontificia Universidad Católica del Perú, Lima, Peru*
[74]*Dipartimento di Fisica dell'Università and Sezione INFN, Trieste, Italy*
[75]*Centro de Investigación y de Estudios Avanzados (CINVESTAV), Mexico City and Mérida, Mexico*
[76]*Universidade de São Paulo (USP), São Paulo, Brazil*
[77]*Dipartimento di Fisica dell'Università and Sezione INFN, Cagliari, Italy*
[78]*Centro de Aplicaciones Tecnológicas y Desarrollo Nuclear (CEADEN), Havana, Cuba*
[79]*Yonsei University, Seoul, South Korea*
[80]*Saha Institute of Nuclear Physics, Kolkata, India*
[81]*Physics Department, Creighton University, Omaha, Nebraska, USA*
[82]*Université de Lyon, Université Lyon 1, CNRS/IN2P3, IPN-Lyon, Villeurbanne, France*
[83]*Division of Experimental High Energy Physics, University of Lund, Lund, Sweden*
[84]*Pusan National University, Pusan, South Korea*
[85]*Sezione INFN, Cagliari, Italy*
[86]*Dipartimento di Scienze e Innovazione Tecnologica dell'Università del Piemonte Orientale and Gruppo Collegato INFN, Alessandria, Italy*
[87]*Benemérita Universidad Autónoma de Puebla, Puebla, Mexico*
[88]*Instituto de Ciencias Nucleares, Universidad Nacional Autónoma de México, Mexico City, Mexico*
[89]*Institute of Space Sciences (ISS), Bucharest, Romania*
[90]*Institut de Physique Nucléaire d'Orsay (IPNO), Université Paris-Sud, CNRS-IN2P3, Orsay, France*
[91]*Bose Institute, Department of Physics and Centre for Astroparticle Physics and Space Science (CAPSS), Kolkata, India*
[92]*Universidade Estadual de Campinas (UNICAMP), Campinas, Brazil*
[93]*Dipartimento di Fisica "E. R. Caianiello" dell'Università and Gruppo Collegato INFN, Salerno, Italy*

[94]*Sezione INFN, Bari, Italy*

[95]*National Centre for Nuclear Studies, Warsaw, Poland*

[96]*Sezione INFN, Rome, Italy*

[97]*Department of Physics, University of Oslo, Oslo, Norway*

[98]*Institute for Nuclear Research, Academy of Sciences, Moscow, Russia*

[99]*Physics Department, University of Athens, Athens, Greece*

[100]*Sezione INFN, Trieste, Italy*

[101]*Chicago State University, Chicago, USA*

[102]*Warsaw University of Technology, Warsaw, Poland*

[103]*Universidad Autónoma de Sinaloa, Culiacán, Mexico*

[104]*Physics Department, University of Rajasthan, Jaipur, India*

[105]*Technical University of Split FESB, Split, Croatia*

[106]*A. I. Alikhanyan National Science Laboratory (Yerevan Physics Institute) Foundation, Yerevan, Armenia*

[107]*University of Tokyo, Tokyo, Japan*

[108]*Department of Physics, Sejong University, Seoul, South Korea*

[109]*Eberhard Karls Universität Tübingen, Tübingen, Germany*

[110]*Institut für Kernphysik, Technische Universität Darmstadt, Darmstadt, Germany*

[111]*Yildiz Technical University, Istanbul, Turkey*

[112]*KTO Karatay University, Konya, Turkey*

[113]*Zentrum für Technologietransfer und Telekommunikation (ZTT), Fachhochschule Worms, Worms, Germany*

[114]*California Polytechnic State University, San Luis Obispo, California, USA*

[115]*The University of Texas at Austin, Physics Department, Austin, Texas, USA*

[116]*M. V. Lomonosov Moscow State University, D. V. Skobeltsyn Institute of Nuclear Physics, Moscow, Russia*

[117]*Institute of Physics, Academy of Sciences of the Czech Republic, Prague, Czech Republic*

[118]*University of Tennessee, Knoxville, Tennessee, USA*

[119]*Dipartimento di Fisica dell'Università "La Sapienza" and Sezione INFN, Rome, Italy*

[120]*University of Belgrade, Faculty of Physics and "Vinča" Institute of Nuclear Sciences, Belgrade, Serbia*

[121]*Indian Institute of Technology Indore, Indore, India (IITI)*

[122]*National Institute of Science Education and Research, Bhubaneswar, India*

[123]*Budker Institute for Nuclear Physics, Novosibirsk, Russia*

[124]*Institut of Theoretical Physics, University of Wroclaw, Wroclaw, Poland*

[125]*Laboratori Nazionali di Legnaro, INFN, Legnaro, Italy*

[126]*Nuclear Physics Group, STFC Daresbury Laboratory, Daresbury, United Kingdom*

[127]*Hiroshima University, Hiroshima, Japan*

[128]*Kirchhoff-Institut für Physik, Ruprecht-Karls-Universität Heidelberg, Heidelberg, Germany*

[129]*Centre de Calcul de l'IN2P3, Villeurbanne, France*